Accepted Manuscript

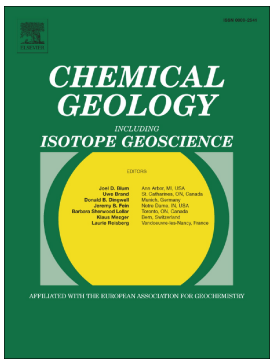

Pargasite in fluid inclusions of mantle xenoliths from northeast Australia (Mt. Quincan): Evidence of interaction with asthenospheric fluid

Márta Berkesi, György Czuppon, Csaba Szabó, István Kovács, Silvio Ferrero, Marie-Christine Boiron, Chantal Peiffert

PII: S0009-2541(18)30325-5
DOI: doi:10.1016/j.chemgeo.2018.06.022
Reference: CHEMGE 18821

To appear in: *Chemical Geology*

Received date: 6 December 2017
Revised date: 8 June 2018
Accepted date: 28 June 2018

Please cite this article as: Márta Berkesi, György Czuppon, Csaba Szabó, István Kovács, Silvio Ferrero, Marie-Christine Boiron, Chantal Peiffert , Pargasite in fluid inclusions of mantle xenoliths from northeast Australia (Mt. Quincan): Evidence of interaction with asthenospheric fluid. Chemge (2018), doi:10.1016/j.chemgeo.2018.06.022

Pargasite in fluid inclusions of mantle xenoliths from northeast Australia (Mt. Quincan): evidence of interaction with asthenospheric fluid

Márta Berkesi[1*], György Czuppon[2], Csaba Szabó[1], István Kovács[3], Silvio Ferrero[4], Marie-Christine Boiron[5], Chantal Peiffert[5]

[1]Lithosphere Fluid Research Lab, Eötvös University Institute of Geography and Earth Sciences, Pázmány Péter sétány 1/c, Budapest H-1117, Hungary

[2]Institute for Geological and Geochemical Research, Research Center for Astronomy and Earth Sciences, Hungarian Academy of Sciences, Budaörsi út 45, Budapest H-1112, Hungary

[3] Geodetic and Geophysical Institute, Hungarian Academy of Science, H-9400 Sopron, Hungary

[4]Universität Potsdam, Institute of Earth and Environmental Science, Karl-Liebknecht-Str. 24-25, Potsdam 14476, Germany

[5]GeoRessources, Université de Lorraine, CNRS, CREGU, BP 70239, 54506,Vandoeuvre-lès-Nancy Cedex, France

*Corresponding author: marta.berkesi@gmail.com

Abstract

Three spinel lherzolite xenoliths from Mt Quincan (Queensland, northeastern Australia) were studied with special attention to their enclosed fluid inclusions. The xenoliths are deformed, have porphyroclastic textures and overall show very similar petrographic features. The only significant difference is manifested in the abundance of fluid inclusions in the samples, mostly in orthopyroxene porphyroclasts. Xenolith JMTQ11 is *fluid inclusion-free*, whereas xenolith JMTQ20 shows a high abundance of fluid inclusions (*fluid inclusion-rich*). Xenolith JMTQ45 represents a transitional state between the previous two, as it contains only a small amount of fluid inclusions (*fluid inclusion-bearing*). Previous studies revealed that these xenoliths and the entrapped fluid inclusions represent a former addition of a MORB-type fluid to the pre-existing lithosphere, resulting from asthenosphere upwelling. There is a progressive enrichment in LREE, Nb, Sr and Ti from the fluid inclusion-free xenolith through the fluid inclusion-bearing one to the fluid inclusion-rich lherzolite. This suggests an increase in the extent of the interaction between the fluid-rich melt and the lherzolite wallrock. In addition, the same interaction is considered to be responsible for the formation of pargasitic amphibole as well.

The presence of fluid inclusions indicates fluid migration at mantle depth, and their association with exsolution lamellae in orthopyroxene suggests fluid entrapment following the continental rifting (thermal relaxation) during cooling. A series of analyses, including microthermometry coupled with Raman spectroscopy, FTIR hyperspectral imaging, and Focused Ion Beam-Scanning Electron Microscopy (FIB-SEM) was carried out on the fluid inclusions. Based on the results, the entrapped high-density fluid is composed of 75-89 mol % CO_2, 9-18 mol % H_2O, 0.1-1.7 mol % N_2 and $\leq$ 0.5 mol % H_2S with dissolved trace elements (melt component).

Our findings suggest that the metasomatic fluid phase could have been either a fluid-rich silicate melt released from the deeper asthenosphere, or a coexisting incipient fluid-rich silicate melt. Further cooling, possibly due to thermal relaxation and the upward migration of the fluid phase, caused the investigated lherzolites to reach pargasite stability conditions. We conclude that pargasite, even if only present in very limited modal proportions, can be a common phase at spinel lherzolite stability in the lithospheric upper mantle in continental rift – back-arc settings. Studies of fluid inclusions indicate that significant CO_2 release from the asthenosphere in a continental rifting environment is resulting from asthenosphere upwelling and its addition to the lithospheric mantle together with fluid-rich melt – lherzolite interaction that leaves a CO_2-rich fluid behind.

Keywords: Fluid inclusions, pargasite, asthenospheric fluid, metasomatism, Mt. Quincan, Australia

Highlights

Multi-technique study on fluid inclusions from upper mantle xenoliths, Mt. Quincan

Significant CO_2 release from the asthenosphere in a continental rifting environment

Metasomatic pargasite is formed during thermal relaxation of the lithosphere

1. Introduction

It is widely accepted that volatiles play a significant role in the subcontinental lithospheric mantle (e.g., Andersen and Neumann, 2001), especially in promoting reactions and/or cause metasomatism either modally (resulting in introduction of new minerals, Harte 1983; O'Reilly and Griffin, 2013) or cryptically (resulting in change of composition without the formation of new phases, Dawson, 1984; O'Reilly and Griffin, 2013). Special attention has been given to fluids in subduction zones and arc magmatism (e.g., Peacock, 1990; Manning, 2004, Kessel et al., 2005) from numerical modelling (e.g., Iwamori, 1998; Gerya et al., 2002) through experimental and thermodynamic approaches (e.g., Keppler 1996; Galvez et al., 2016) and implications to the fluid flow (e.g., Spandler et al., 2011; John et al., 2012) to inclusion studies (e.g., Scambelluri and Philipot 2001; Scambelluri et al., 2015). All these works focus on the understanding of fluids that might have been released from the slab (e.g., Tumiati et al., 2017) and percolate further into the mantle wedge (Ayers, 1998), triggering melting (e.g., Kessel et al., 2005).

There are only a few papers discussing fluids that potentially reacted with mantle peridotites during continental rifting (Griffin et al., 1984; Andersen et al., 1984, Frezzotti et al., 2010; Pintér et al., 2015, Park et al., 2017). Studies of lherzolites from extensional tectonic settings suggest that portions of the lithospheric mantle or the asthenosphere could contain a significant amount of pargasitic amphibole (e.g., Fumagalli et al., 2009; Frezzotti et al., 2010; Pintér et al., 2015) in some cases with high Cr-Na formed from a hydrous hybrid MORB melt (Borisova et al., 2012). The eastern margin of Australia provides a great opportunity to study mantle xenoliths in a continental rift setting and to extend our knowledge on the role of fluids in pargasite formation. Mantle xenoliths from Victoria (southeastern Australia) indicate that the reacting fluid or fluid-rich melt

was generated in the garnet lherzolite stability field (Andersen et al., 1984) or has been recycled from an altered oceanic crust. In contrast, fluids found in Mt. Quincan xenoliths (Queensland, northeastern Australia) were proposed to have asthenospheric origin based on their noble gas content (Czuppon et al., 2009). The asthenosphere can be a potential reservoir for fluid and incipient melt (Green et al., 2010; Green, 2015) outside of the pargasite stability field, and such fluids can then be entrapped in the lithosphere after a part of the asthenosphere is subcreted to the base of the lithosphere (e.g., Pintér et al., 2015).

Fluids at upper mantle depth are likely CO_2-rich as proven by previous fluid inclusion studies (e.g., Frezzotti and Touret, 2014 and references therein), in accordance with the significant CO_2 fluxes observed in continental rift zones (Robertson et al., 2016; Lee et al., 2017). Fluid composition is variable, with C-O-H-N-S as main components and it may additionally contain a dissolved silicate melt component (Berkesi et al., 2012).

Here we report a detailed study on fluid inclusions in spinel lherzolite xenoliths from Mt. Quincan, Queensland, northeastern Australia. Such inclusions are remnants of an asthenosphere derived (CO_2-H_2O-bearing) fluid-rich melt, that may be also responsible for metasomatizing the spinel lherzolites during thermal relaxation, followed by the asthenosphere upwelling which then led to the formation of pargasite.

2. Geological setting and sampling

Xenoliths in this study were collected from the scoria cone of Mt. Quincan, in the <3 Ma Atherton Tablelands Volcanic Province (ATVP), which is located within the Hodgkinson Fold Belt, a part

of the eastern Australian composite Phanerozoic Tasman Fold Belt (Fig 1 in Handler et al., 2005). The ATVP covers an area of ~1800 km^2 with 52 known eruptive centers (Stephenson, 1989).

The geologic evolution of the Hodgkinson Fold Belt has been dominated by subduction during the middle Ordovician (Donchak, 1997). Starting in the Mesozoic, major tectonic processes involved rifting and associated seafloor spreading along the margin of the Australian craton. This was controlled by slab rollback and back-arc extension processes (Allen et al. 1997; Schellart et al. 2006; Kositcin et al. 2009). The present tectonic setting of northeastern Australia is a passive continental margin due to the opening of the Tasman Sea (Handler et al., 2005). The western part of the Hodgkinson Fold Belt terminates at the Tasman Line (Hill, 1951), which separates the Hodgkinson Fold Belt from the Precambrian Georgetown Inlier, possibly with a lithosphere-scale fault system (Kennett et al., 2004; Fishwick et al., 2008).

During the Cenozoic, continued extension resulted in the formation of widespread intraplate basalt fields (Murgulov et al., 2012), transporting numerous mantle-derived xenoliths to the surface along the eastern margin of Australia (O'Reilly, 1988). The ages of the ATVP volcanic forms vary between 10 ka and 3 ka, and the pyroclastic cone of Mt. Quincan is known to enclose abundant granulite and spinel lherzolite xenoliths (Stephenson 1989).

Major and trace element geochemical data, together with combined Sr, Nd and Os isotopic composition of whole rocks from the spinel lherzolite suite from Mt Quincan suggest variable degrees of melt extraction at around 275 Ma from a depleted MORB mantle- (DMM-) like source (Handler et al., 2005). Isotope data shows only minimal (if any) signs of subduction-related fluids/melts in the genesis or subsequent modification of the shallow lithospheric mantle.

In addition, helium, argon and xenon compositions of the xenoliths from Mt Quincan indicate the preservation of a MORB-like character in a relatively recent fluid entrapment, which might be related to the rifting of Eastern Australia after the Paleozoic subduction events (Czuppon et al., 2009). Extreme high density (≥1 g/cm^3) fluid inclusions in one xenolith from Mt. Quincan were found to be containing a small amount of N_2 (Berkesi et al., 2017), supporting the idea that the presence of nitrogen in a free fluid phase in the subcontinental lithospheric mantle could be more common than previously thought.

3. Analytical techniques

Three spinel lherzolites (JMTQ11, JMTQ20 and JMTQ45), - two of them enclosing fluid inclusions (JMTQ20 and JMTQ45) -, were chosen for microscopic and spectroscopic analyses. Double-polished thick sections (~100 μm) were prepared from the xenoliths, and various fluid inclusions close to the surface (<10 μm) were selected for further analyses.

Microthermometric data were collected using a Linkam THMS600 heating-cooling stage mounted on a Nikon Eclipse LV100PL polarizing microscope at the Lithosphere Fluid Research Lab, Eötvös University, Budapest. For calibration, we used the melting point of CO_2 at –56.6 ºC, with the accuracy of ±0.1 ºC. The fluid inclusions were cooled below complete freezing (between -90 and -100 ºC), then slowly heated (1 °C/ min) until visible homogenization (liquid + vapor → liquid) occurred. The density and minimum pressure values of the fluids were estimated using the FLUIDS software package (BULK & ISOC) (Bakker, 2003). Micro-Raman analysis was conducted to determine fluid components at the Faculty of Science Research and Instrument Core

Facility of Eötvös University, Budapest (ELTE FS-RICF). We used a confocal HORIBA Labram HR (high resolution) 800 spectrometer with Nd:YAG laser (λ = 532 nm) excitation, 1800 gr/mm optical grating, a 50–200 μm confocal hole, 2–100 s acquisition time, and a 100× objective. The laser spot size (lateral) was measured to be 1.17 μm, and the depth resolution was 1.73 μm (using a 50 μm confocal hole and 100× objective). The laser power was 130 mW at the source and ~50 mW at the sample surface. The spectral resolution was 0.7 cm^{-1} at 1398.5 cm^{-1} (full width at half maximum of one neon line). Data evaluation (background fitting and peak fitting using the Gaussian–Lorentzian sum profiles) was carried out using LabSpec software. For mineral and fluid identification, the databases of Frezzotti et al. (2012a) and RRUFF (rruff.info) were used.

At ELTE FS-RICF, focused ion beam–scanning electron microscopy (FIB–SEM) analyses were conducted as well, using a FEI QUANTA 3D FIB–SEM apparatus equipped with both secondary and backscattered electron (BSE) detectors, together with a silicon drift energy dispersive spectrometer (EDS). Fluid inclusions with size between 5–25 μm and situated less than 5 μm from the surface were selected for FIB–SEM analysis. The accelerating voltage and current of the electron beam were 20 kV and 10 nA, respectively, which allowed major elements with masses ranging from those of beryllium through oxygen to barium to be analyzed. Identification of the daughter phases was based mostly on their morphology on the secondary electron images and their brightness on the BSE images, along with the examination of their EDS spectra. Because of the small size of the daughter phases in the inclusions (1–5 μm), the signals detected by EDS were mixed signals, as X-rays from adjacent areas (host phase and/or other daughter minerals) were also recorded. To distinguish the daughter phase signal from that of the host mineral, EDS control spectra for the host mineral were acquired in the proximity and from the same depth after each acquisition of a daughter mineral spectrum. The detailed methodology for this technique is

described in Berkesi et al. (2012). The step size for the FIB slicing of the fluid inclusions was set to 200 nm.

In order to obtain the major element composition of orthopyroxene porphyroclasts and their enclosed lamellae, electron microprobe analyses (EPMA) were conducted using a wavelength-dispersive JEOL JXA-8200 electron microprobe at the Institute of Earth and Environmental Science, Universität Potsdam with instrument settings of 15 kV accelerating voltage, 15 nA beam current, 2 μm beam size and 20 s counting times. Natural standards were used for the analyses and ZAF correction was applied.

Volume percentages of clinopyroxene and spinel lamellae in the orthopyroxenes were calculated using one to three representative BSE images for each xenolith. Image resolutions were 254 dpi with a pixel number of 1280x960. Corel PHOTO-PAINT v.X8 was used to calculate the pixel numbers of the phases. The pixel number of all orthopyroxene porphyroclast, clinopyroxene and spinel lamellae was taken as the volume percentage.

Hyperspectral imaging based on infrared analysis was performed on the fluid inclusions to search for infrared active components (H_2O, OH^- and CO_2) in the inclusions (ELETTRA Synchrotron Light Laboratory of Trieste, Italy). For the hyperspectral images we used a globar light source with an FPA detector and 5×5 μm aperture or synchrotron source with MCT detector and 8×8 μm aperture. Hyperspectral infrared maps were obtained by integrating the absorbance spectra after baseline subtraction, usually in the 3000–3700 cm^{-1} spectral range for molecular water (referred to as H_2O for short), 3700-3720 cm^{-1} for pargasite and 2300–2450 cm^{-1} for CO_2.

Laser ablation inductively coupled plasma mass spectrometry (LA-ICP-MS) analyses have been carried out in order to determine the concentration of major and trace elements of the constituent

minerals of the xenoliths and their enclosed fluid inclusions. The LA-ICP-MS instrument (GeoRessources laboratory, Nancy, France) comprises a GeoLas excimer laser (ArF, 193nm, Microlas, Göttingen, Germany) and an Agilent 7500c quadrupole ICP-MS. More details on the LA-ICP-MS experimental system and the applied calibration procedure are given in Leisen et al. (2012). During the analyses, the following parameters were used: 1.2 l/min He-flow with 10–50 μm spot size, 0.01 s dwell time, 5 Hz repetition rate. For external standardization, NIST reference glass standards SRM 610 and SRM 612 were used. Data processing was carried out using the IOLITE software (Paton et al., 2011). For trace element analyses of the pyroxene hosts, microscopic examinations were carried out to make sure no crystal and/or silicate melt inclusion fell within the ablation volume. For fluid inclusion analyses, the beam size was always set to be greater than the diameter of the fluid inclusion (>10 μm) in order to sample the entire inclusion plus some of the host. The following isotopes were monitored for in situ fluid inclusion ablation: ^{23}Na, ^{24}Mg, ^{29}Si, ^{39}K, ^{43}Ca, ^{85}Rb, ^{88}Sr, ^{89}Y, ^{93}Nb, ^{137}Ba, ^{139}La, ^{140}Ce, ^{146}Nd, ^{147}Sm, ^{208}Pb, ^{232}Th, ^{238}U. For clinopyroxene and pargasite, the same isotopes were analyzed with the addition of ^{47}Ti, ^{53}Cr, ^{57}Fe, ^{60}Ni, ^{63}Cu, ^{90}Zr, ^{93}Nb, ^{137}Ba, ^{141}Pr, ^{153}Eu, ^{157}Gd, ^{159}Tb, ^{163}Dy, ^{165}Ho, ^{166}Er, ^{169}Tm, ^{172}Yb and ^{175}Lu.

4. Xenolith petrography

The Mt. Quincan xenoliths are fresh spinel lherzolites ranging in size from ca. 10 to 25 cm in diameter. For the analyses, we selected parts of the xenoliths without any visible petrographic sign of infiltration by the host basalt, which is regularly restricted to the outermost few millimeters of

the xenoliths (Handler et al., 2005). The samples are part of the xenolith series studied by Handler et al., 2005 and Czuppon et al., 2009, and they were described as group-I spinel lherzolites having porhyroclastic texture with mainly orthopyroxenes and subordinately olivines as porphyroclasts (up to 3 mm in size) (Fig.1a). Modal compositions of the studied xenoliths vary in narrow range, with 61 – 65 % olivine, 19 – 22 % orthopyroxene, 9 - 12 % clinopyroxene, 2 – 4 % spinel and ≤1 % amphibole.

Clinopyroxene and spinel are present only as small euhedral or anhedral crystals (up to 1 mm, Fig. 1a), however, non-lamellar clinopyroxene and spinel are not associated to each other. In other words, they are not the crystal inclusion to one another. Fine exsolution lamellae of clinopyroxene and spinel can be observed in euhedral orthopyroxene porphyroclasts (Fig. 1 b and c), and orthopyroxene and spinel lamellae appear in clinopyroxene porphyroclasts (Fig. 1d) and medium sized neoblasts. The volume proportion of clinopyroxene and spinel lamellae compared to the enclosing orthopyroxene porphyroclasts are 1.7-2.3 ±0.1 % and 0.3-0.5 ±0.1 %, respectively. The enclosing orthopyroxene varies between 97.0-98.0 ±0.1 vol. % (where lamellae occur). In clinopyroxene neoblasts, the amount of exsolution lamellae are 1.1-1.9 ±0.1 vol. % for orthopyroxene and 0.3-0.5 ±0.1 vol. % for spinel. Olivine porphyroclasts show undulose extinction. Grain boundaries vary from straight to curved, and locally form triple junctions.

Fluid inclusions have different abundance in the three samples, with increasing amount from JMTQ11 (fluid inclusion-free) through JMTQ45 (fluid inclusion-bearing) to JMTQ20 (fluid inclusion-rich). The fluid inclusions are generally found in the orthopyroxene porphyroclasts (Fig 1b and d) and subordinately in clinopyroxenes. The appearance of the fluid inclusions suggests one fluid invasion event recorded in the studied xenoliths. Moreover, as they are always aligned parallel to the lamellae in the orthopyroxene porphyroclasts and never reach the edge of the host

crystal (Fig 1b and f), they can be regarded as the result of early trapping (Touret, 2001). The inclusions show negative crystal shape with variable sizes ranging between 3 - 70 μm, and they are dominantly consisting of liquid and solid phases (on the inclusion walls) at room temperature (Fig 1e). It is noteworthy that no melt inclusions were found in the xenoliths.

Crystal inclusions such as pargasite, with sizes up to 120 μm, are present in both ortho- and clinopyroxenes only in fluid inclusion-bearing samples (JMTQ20 and JMTQ45) (Fig. 1d). Although pargasite is minor component in both xenoliths, its modal proportion increases from the fluid inclusion-bearing to the fluid inclusion-rich sample.

5. Composition of peridotites

Major element compositions of the constituent minerals are given in Table 1. No geochemical zonation or compositional difference between lamellae and rock-forming pyroxenes was observed. The Mg# [Mg/(Mg+Fe) in a.p.f.u] of both olivine and pyroxenes range between 0.89 and 0.91 (Table 1), and the Cr# of spinel varies between 0.11 and 0.14 (Cr/(Cr+Al) in a.p.f.u., Table 1). The Mg# of olivine and the Cr# of spinel is close to the fertile MORB mantle (FMM) composition (Arai, 1994), indicating a maximum of only ~3**%** of melt extraction (Fig 2). Olivine contains 0.39-0.41 wt.% NiO, Al_2O_3 in orthopyroxene and clinopyroxene varies between 4.1-5.3 and 5.2-6.9 wt.%, respectively. From fluid inclusion-free through fluid inclusion-bearing to fluid inclusion-rich xenoliths, Al_2O_3 concentration in clinopyroxene is increasing (from 6.9 to 5.2 wt. %), whereas Na_2O is slightly decreasing (from 1.3 to 0.9 wt. %) (Table 1). Pargasite inclusions in clinopyroxene

of lherzolite JMTQ20 have average Na_2O and TiO_2 concentrations of 3.2 wt. % and 1.4 wt.%, respectively (Table 1), and they contain no or only a very small amount of Cl (≤0.02 wt. %).

Clinopyroxene and pargasite (only in xenolith JMTQ20, Table 2), as main containers of trace elements, reflect metasomatic imprints correlated with the abundance of fluid inclusions. Clinopyroxene in the fluid-free xenolith (JMTQ11) contains the lowest amount of trace elements, especially Ba, Zr and LREE (Fig 3a). In contrast, the fluid-bearing xenolith (JMTQ45) shows elevated concentrations for U, Ba, Nb and LREE (Fig 3a and c) in clinopyroxene. Trace element, especially REE patterns (Fig 3c) of pargasite and clinopyoxene in the fluid inclusion-rich xenolith (JMTQ20) indicate a fertile composition. Compared to clinopyroxene, pargasite is enriched in Rb, Ba Nb and Ti, which are known to prefer partitioning into pargasite at mantle depth (Ionov and Hoffmann, 1995) (Fig 3b). The average ratio of La_N/Lu_N in clinopyroxene varies from 0.001 through 0.28 to 1.15 in the fluid inclusion-free, fluid inclusion-bearing and fluid inclusion-rich samples, respectively (Table 2).

6. Composition of fluid inclusions

6.1. Microthermometry and Raman spectroscopy

The results of the measurements on fluid inclusions are listed in Table 3. A minor part of the microthermometric data has been published by Berkesi et al. (2017), revealing high-density (≥1 g/cm^3) CO_2-rich fluids in JMTQ45. Additional analyses in the same sample, along with the fluid inclusion-rich JMTQ20 peridotite, confirmed this finding. Melting temperatures of the carbonic phase vary between -57.4 °C and -56.8 °C in JMTQ45, and between -57.5 °C and -56.5 °C in

JMTQ20. Upon further heating, carbonic phase in fluid inclusions homogenized to liquid phase between -34.2 °C and -5.1 °C in JMTQ45, and between -35.2 °C and -8.9 °C in JMTQ20 (Table 3), showing a positive correlation with their size; i.e., the smaller the inclusion, the lower was the homogenization temperature.

Detailed Raman spectroscopy at room temperature proved the presence of additional fluid components besides CO_2, such as N_2 (Raman band at 2327 cm^{-1}, Berkesi et al., 2017), H_2S (Raman band at 2608 cm^{-1}) (Fig 4a and b) and very rarely, liquid H_2O (Fig. 5) when focusing at the inclusion wall with the exciting laser. However, upon heating, the Raman analysis revealed the presence of H_2O in each fluid inclusion appearing as a characteristic symmetric band, with a peak position varying between 3629 - 3636 cm^{-1} (Fig. 5), which corresponds to dissolved H_2O in the CO_2-rich phase.

We measured total homogenization temperatures of the fluid inclusions (i.e., the temperature at which only a single fluid phase is in equilibrium, as there is no longer immiscibility between the CO_2 and the H_2O-rich phase, Fig. 6). Molar percentages of the fluid species were calculated from the spectra recorded at, or higher than, the total homogenization temperature. Starting from 25 ºC, spectra were acquired focusing the laser on the CO_2-rich liquid phase. The inclusions were then heated gradually and analyzed at steps of 25 ºC. At each step, we checked the proportion of the total integrated band of the CO_2 range (including the Fermi diad and the hot bands; Rosso and Bodnar, 1995) compared to the integrated band area of the dissolved H_2O (Fig. 6). This ratio was continuously decreasing during heating until the inclusions reached their total homogenization temperature, beyond which no further change in the ratio was observed (Fig. 6). Molar percentages of the fluid molecules were calculated within each individual fluid inclusion at the point of their total homogenization. A similar method for quantifying the amount of methane in water was

previously reported by Pironon et al. (2003). Total homogenization temperatures of the fluid inclusions fall between 75 and 125 ºC, and the average composition of the homogeneous fluid is 94 mol % CO_2, 3-6 mol % H_2O, 0.3-2.1 mol % N_2 and up to 0.5 mol % H_2S (Table 3).

The solid phases (Fig. 7) were identified as magnesite (based on its Raman bands at 1094, 738 and 330 cm^{-1}; Fig. 7b) in the orthopyroxene-hosted fluid inclusions, and dolomite (bands at 1099 and 723 cm^{-1}) and pargasite (band at 3690 cm^{-1}, Fig. 7a) in the clinopyroxene hosted fluid inclusions in both fluid inclusion-bearing xenoliths. In addition, α-quartz was found coexisting with magnesite in the orthopyroxene-hosted fluid inclusions, based on its peak at 464 cm^{-1} (Fig. 7b).

6.2. FTIR hyperspectral imaging

Infrared hyperspectral images (maps) in the orthopyroxene-hosted fluid inclusions were acquired both in JMTQ45 (n=2) and JMTQ20 (n=2) xenoliths to obtain the spatial distribution of IR active phases within the fluid inclusions (Fig. 8a). Characteristic bands of the host in the 3000-3700 cm^{-1} range were detected at 3600 and 3520 cm^{-1}, which are well-known as structural hydroxyl incorporated in orthopyroxene (e.g., Ingrin and Skogby, 2000; Peslier et al., 2002; Skogby, 2006; Sundvall and Stalder, 2011). The hyperspectral images revealed the distribution of CO_2 (band at 2344 cm^{-1}, Fig. 8c) and H_2O in liquid form (broad band between 3000 and 3750 cm^{-1}), the latter probably occurring at the walls of the inclusions (Fig. 8b). The bands at 3712 cm^{-1} and ~3670 cm^{-1} in the inclusions are associated with OH-stretching vibrations of pargasite (Jenkins et al., 2003; Della Ventura et al., 2003) (Fig 8b and e).

6.3. Focused ion beam-scanning electron microscopy (FIB-SEM)

We carried out FIB-SEM slicing on representative orthopyroxene-hosted fluid inclusions to measure the precise volume percentages occupied by the different solid phases, following the procedure of Berkesi et al. (2012). Magnesite, quartz and pargasite are all euhedral, with sizes ranging between 1-3 μm, 1.5-2.5 μm and 3-5 μm, respectively (Fig. 7). On the wall of the orthopyroxene-hosted fluid inclusions in the JMTQ20 xenolith, a 2-2.5 μm sized euhedral Fe-Ni sulfide was also identified (Fig. 9).

Based on the SEM images taken at equal distance steps and the method described by Anderson and McCarron, 2011, the proportion of magnesite within the inclusion cavity ranges from 3.1 to 5.2 vol. % (3.7–4.8 vol. % in JMTQ45 and 3.1–5.2 vol. % in JMTQ20; Table 3). The volume of quartz ranges from 2.0 to 3.3 vol. % (2.0–2.8 vol. % in sample JMTQ45 and 2.6–3.3 vol. % in sample JMTQ20, Table 3), whereas pargasite ranges between 12.7 and 16.0 vol. % (13.0-15.3 vol. % in JMTQ45 and 12.7-16.0 vol. % in JMTQ20, Table 3). The volume percentage of sulfides within the fluid inclusions is 0.7-0.8 vol. %.

6.4. LA-ICPMS of the fluid inclusions

Trace element contents of the fluid inclusions were analyzed by in situ LA-ICP-MS analysis in the fluid inclusion-bearing xenolith JMTQ45 and the fluid inclusion-rich JMTQ20. For these analyses, we selected a laser spot size large enough to include the entire volume of the inclusion, plus some of the surrounding host mineral. This approach ensured that any elements associated with the trapped fluid, whether in the fluid phase or deposited on the walls of the inclusion during post-entrapment processes, were included in the analyzed volume. A clear increase was observed for some trace elements compared to concentrations in the host orthopyroxene in xenoliths JMTQ45

and JMTQ20 (Fig. 10). The duration of the mixed host - fluid inclusion transient signal was typically 5–8 s (Fig 10) and sodium, Sr and Ce showed slight increase in signal intensity while the fluid inclusions were being ablated (Fig. 10).

7. Discussion

7.1. The metasomatic fluid

The xenoliths characterized in this study were the part of the same sample series of Czuppon et al. (2009), who proposed an asthenospheric origin for the fluids from the Mt. Quincan spinel lherzolite xenoliths based on the MORB-like noble gas compositions. Our microscopic observations on the same set of samples reveals only one fluid infiltration event, thus suggesting that the fluid inclusions we have investigated are responsible for the asthenospheric noble gas signature reported by Czuppon et al (2009).

The composition of the metasomatic fluid was inferred from the fluid inclusion data and the chemical compositions of the modal metasomatic products (i.e. pargasite) and cryptically altered clinopyroxene. In the inclusions, the CO_2-rich phase represents the residual fluid left behind after a two-stage process: (1) fluid-rock interaction leading to cryptic metasomatism in clinopyroxene and the formation of pargasite, and (2) formation of daughter and step-daughter phases within the inclusion cavity following fluid entrapment (e.g., carbonates, quartz, Fig. 7). Post-entrapment crystallization of the daughter minerals is supported by their constant volume percentages. Furthermore, the formation of magnesite and quartz in orthopyroxene-hosted, or dolomite and quartz in clinopyroxene-hosted fluid inclusion cannot take place at mantle temperatures (e.g.,

Berkesi et al., 2012; Frezzotti et al., 2012b) further supporting the idea of their secondary formation.

Using the method of Andersen et al. (1984), the composition of the entrapped fluid was calculated combining the density data from microthermometry, the mol % composition of the homogenized fluid phase, and the volume percentages of the secondary solids. The resulting fluid composition is: 75-89 mol % CO_2, 9-18 mol % H_2O, 0.2-1.7 mol % N_2 and ≤ 0.5 mol % H_2S, in addition to noble gases based on the previous study of Czuppon et al. (2009 (Table 3). It must be noted that the bulk sulfur content may be higher, as indicated by the presence of sulfides (Fig. 9). Such fluids could have been locally abundant in the asthenosphere beneath the studied area. It is noteworthy that post-entrapment modifications such as partial decrepitation, selective water leakage through micro- or even nanometer scale dislocations (Viti and Frezzotti, 2000), and H_2 diffusion may result in underestimation of the H_2O content for the entrapped fluid (Frezzotti and Peccerrilo, 2007). Besides these possibilities, nevertheless, the combination of moderately high temperature Raman spectrosocopy and volume proportions of secondary solids from FIB-SEM analyses provided a unique opportunity to determine the fluid inclusion composition with high precision.

As it is evident from the previous paragraph the investigated fluid inclusions do not contain Cl (Table 2), although it would be expected during metasomatic events which result paragasite formation, as it has been proposed that Cl (besides of H_2O) plays a significant role in pargasite formation in the spinel lherzolite stability field in general (Frezzotti et al., 2010). The trace element patterns of clinopyroxene and pargasite in the investigated xenoliths (Fig. 3) further support the absence of Cl. The dissolved chlorine at upper mantle pressures (1-2 GPa) would strongly increase the solubility of Pb (and other metals) in the fluid and cause a depletion in HFSE (High Field Strength Elements; Keppler, 1996; Manning, 2004, Frezzotti et al., 2010). However, we observed

high concentrations of HFS elements (Nb, Zr and Ti) in both clinopyroxene (Fig. 3a) and pargasite (Fig 3b) besides the enrichment of LILE (Large Ion lithophile Element: Rb, Ba) and LREE (Light Rare Earth Element, especially La and Ce).

The relatively high concentrations of HFSE suggests that the metasomatic agent was a silicate melt, as HFSE prefer to partition into the silicate melt (e.g., Green et al., 1989) by orders of magnitude higher than into the coexisting fluid phase (Young and Lee, 2009). In addition, Young and Lee (2009) showed that if HFSE are added to mantle pyroxenes via cryptic metasomatism, then the metasomatic agent must be a silicate melt. We have observed, however, that the volatile components (CO_2-H_2O-N_2) are the volumetrically dominant one in the fluid inclusions and in case of the entrapment of a fluid-saturated melt the solid phases should be dominant. Melt component is represented by pargasite and probably the sulfides, and their total volume percentage is maximum ~17 vol.%. Dissolved silicate melt component in a CO_2-rich high-density fluid was previously proven to be able to cause cryptic metasomatic overprint in spinel lherzolite xenoliths from the Central Pannonian Basin (Berkesi et al., 2012). Moreover, Wendlandt and Harrison (1979) showed that a CO_2 vapor in equilibrium with a silicate melt would be enriched in LREE. A dissolved silicate melt component can also indicate the original H_2O content of the mantle fluid, as H_2O enhances the solubility of aluminosilicate polymers in the fluid (Manning, 2004). Aqueous fluid with dissolved silicate melt can then dissolve C (graphite) and thus gain a significant control on the CO_2 concentration at slab-mantle interface (Tumiati et al., 2017).

In summary, the metasomatic agent that altered the composition of clinopyroxene and formed pargasite was most likely a fluid phase with dissolved silicate melt. The high concentration of incompatible elements in pargasite relatively to clinopyroxene and other minerals in the lherzolite suggests that crystallization of pargasite extracted the H_2O and the trace elements from this fluid

phase. This resulted in a residual composition rich in volatiles, especially CO_2, which can be commonly found as entrapped fluid inclusions (Roedder, 1984; Frezzotti and Touret 2014). A similar mechanism was suggested for the spinel lherzolite stability field beneath Victoria, southeast Australia, where it was however probably restricted to meter- rather than kilometer-scale (Andersen et al., 1984).

7.2. Driving force and P-T path of the metasomatism

The porphyroclastic texture, as well as the presence of olivines with undulose extinction, indicate that the lherzolites went through deformation (e.g., Mercier and Nicholas, 1975; Ferrando et al., 2008), resulting in formation of porphyroclasts of orthopyroxene. The presence of lamellae in orthopyroxene porphyroclasts (Fig. 1b and c) are indicative of a subsequent cooling at mantle depth (e.g., Bedini et al., 1997). Indeed, the strong T-dependence of Ca-isopleths in orthopyroxene (e.g., Gasparik, 2000) requires clinopyroxene and associated Al-bearing phases such as spinel to be formed as lamellae (Spengler et al., 2012). Consequently, the peridotites show imprints of thermal re-equilibration from higher to lower temperatures. The equilibrium temperatures representing the latest conditions were calculated using the two-pyroxene thermometer of Brey and Köhler (1990), and they show lower temperatures for JMTQ11 (940±16 °C) and higher temperatures for JMTQ20 and JMTQ45 (1031 and 1037±16 °C) at the estimated pressure of 1.5 GPa. We reconstructed lamellae-bearing ortho- and clinopyroxene compositions and calculated temperatures prior to lamellae formation (referred to as 'paleo'-temperatures in Falus et al., 2000). Paleo-temperatures indicate cooling by ~80-100°C in all xenoliths (Fig. 11): from temperatures of 1051±16 °C, 1113 ±16 °C and 1112 ±16 °C for the fluid inclusion-free (JMTQ11), fluid inclusion-bearing (JMTQ45) and fluid inclusion-rich (JMTQ20) xenoliths, respectively.

The lack of inclusions in both the orthopyroxene neoblasts and in the majority of clinopyroxene suggests that the entrapment of the inclusions occurred prior to or simultaneously with the deformation. Negative crystal shape (Fig. 1 e), along with the high fluid density ($\geq$1 g/cm^3) are evidences for textural equilibrium reached after fluid entrapment at mantle depth (e.g., Roedder, 1984; Berkesi et al., 2012; Frezzotti and Touret, 2014). In addition, similarly to the observations of Park et al. (2017), fluid entrapment could have taken place prior to or during lamellae formation. This could be explained either by a fluid invasion event or simply by cooling below the pargasite dehydration solidus temperature at ~1050 °C during thermal relaxation, when the system becomes subsolidus and the small amount of partial melt present precipitates pargasite (Fig. 12).

In the first case of fluid invasion, the metasomatism would be associated with a single metasomatic event from an external fluid that resulted in a progressive increase in 1) LREE, Sr and HFSE (Nb and Zr) in clinopyroxenes (Fig. 3a and c) and 2) slight increase of the modal proportion of metasomatic pargasite, both depending on the amount of the fluid interacting with the spinel lherzolites. All these petrographic and geochemical evidences indicate progressive metasomatism (definition by Huang et al. 2012). As the relative proportion of the metasomatizing fluid can be approximated by the amount of the entrapped fluid inclusions (Berkesi et al., 2012) we compared the abundance of the fluid inclusion in the samples with different concentration of LREE and HFSE as well as pargasite. It appears that the pargasite presents in the samples which contain fluid inclusions and its abundance increases with the amount of fluid inclusions which are typically found along along the clinopyroxene lamellae. In addition, it is important to emphasize that the fluid inclusions also contain pargasite as daughter phase. Alongside the abundance of pargasite, the studied sample also show an increase in LREE, Sr and HFSE (Nb and Zr) in clinopyroxenes, indicating a relationship between the processes that are responsible for the formation of the fluid

inclusion and pargasite and trace element systematics, thus suggesting a common metasomatic event.

In the second case, i.e., fluid entrapment as result of cooling below pargasite dehydration solidus temperature, at paleo-temperatures characteristic for the JMTQ45 and JMTQ20 xenoliths the metasomatic agent could be the incipient fluid-rich melt. These paleo-temperatures exceed the pargasite dehydration solidus (~1050-1100 ^{0}C; Green et al., 2010; Kovács et al., 2012; 2017) at pressures below 3 GPa, which can be safely assumed for the depth of origin of the studied samples (Fishwick et al., 2008). The third sample, xenolith JMTQ11, was always below the pargasite dehydration solidus and the presence of a fluid-rich silicate melt is rather unlikely, which is consistent with the fluid-free nature of this specimen. For the former two samples with higher paleo-temperatures, fluid-rich 'incipient' silicate melt gradually reacted with its host peridotite, forming pargasite and facilitating the exsolution of other phases as the temperature decreased below the amphibole stability (e.g. Kang et al., 2017). Pargasite formation, therefore, used up 'water' which was present in the fluid-rich melt: a process closely resembling metasomatism but occurring without the involvement of external fluids or melts. The presence of fluid inclusions in these samples is thus a direct evidence for the presence of a fluid-rich melt. The driving force of the process is assumed to be the decreasing temperature in the thermal relaxation stage following the extension (Fig. 12), when the incipient melt-bearing lithosphere entered the amphibole stability field. The process can potentially take place in any extensional regime in the upper mantle, where higher temperature isotherms are shifted to lower pressure, followed by thermal relaxation in order to achieve steady-state temperatures. During this process, the melt-bearing part of the upper mantle can cool below the amphibole dehydration solidus, resulting in the consumption of the partial melt and the crystallization of amphibole (e.g. Kovács et al. 2017). Although we cannot exclude

autometasomatism as a responsible process for the observed systematics, it is more likely that an external fluid invasion caused the metasomatism.

Thus, pargasite is likely to have been formed via cooling from the "paleo"-temperatures (~1100 °C) to present equilibration temperatures (around 1030 °C) of the lherzolites, alongside the entrapment of fluid inclusions by interaction of the fluid and the upper mantle. The idea is supported by the pargasite stability (pargasite dehydration solidus) in the MORB pyrolite system (Niida and Green, 1999; MPY on Fig. 11) as well, which terminates between 1050 and 1090 °C in the pressure range characteristic for spinel lherzolite stability. Furthermore, the amount of Na in pargasite is depending not only on temperature, but also on pressure (Niida and Green, 1999), and this relationship can be applied to infer the pressure based on the Na patterns, indicating 12-19.5 kbar for the fluid-invasion event in the lithospheric upper mantle.

7.3. Mantle fluids in the lithospheric mantle in extensional setting

In a rifting environment, asthenosphere upwelling usually results in the upward movement of the isotherms to shallower regions of the lithospheric mantle (Zorin and Lepina, 1985) (Fig. 12), where portions of the uprising asthenosphere can cause thermal erosion and/or geochemically alter the mantle lithosphere (Ewart et al., 1982). Following the asthenospheric upwelling, thermal relaxation causes the lithosphere to thicken (Rey, 2001). As discussed before, the fluid phase in our studied xenoliths could have been trapped before or during cooling-induced lamellae-formation in the orthopyroxene porphyroclasts. In other words, the incipient fluid-rich melt released from the upwelling asthenosphere percolated into the spinel lherzolite stability field during its upward migration. As a consequence of thermal relaxation and possible migration, the

fluid-rich melt metasomatized the surrounding peridotite, leading to the enrichment of incompatible elements as seen in clinopyroxene compositions (Fig. 3a). At the same time, pargasite was formed upon reaching the pargasite stability field as a result of the temperature decrease (Fig. 12). Geophysical data is in good accord with our model. Fishwick et al. (2008) published detailed seismic surface wave tomography and made calculations of the horizontal gradient of shear wave speed throughout the Australian continent and adjacent oceanic lithosphere. It has been revealed that the easternmost block is very thin, of about ~50-60 kilometers with no thermal indication of a plume beneath eastern Australia. Instead, rifting was controlled by slab-rollback and back-arc extension started in the Mesozoic and continued to the Cenozoic as presumed by numerous previous studies (e.g., Allan et al. 1997; Schellart et al. 2006; Kositcin et al. 2009; Murgulov et al., 2012). Such thinned lithosphere is consistent with our model, that supports continental extension and possibly following thermal relaxation.

Fluid inclusions in porphyroclastic lherzolite xenoliths at continental rift settings, with modal pargasite and/or phlogopite and porphyroclasts enclosing exsolution lamellae, have been previously reported in numerous studies, namely from southeast Australia (Griffin et al., 1984; Andersen et al., 1984), Africa (Injibara, Ethiopia: Frezzotti et al., 2010; Cameroon Volcanic Line, Cameroon: Pintér et al., 2015) and North-America (Rio Grande Rift: Park et al., 2017). The similarities in both the lherzolite petrography and the presumed mechanism of the fluid metasomatism suggest that portions of the upper mantle or asthenosphere may contain large reservoirs of free fluid and/or fluid-rich melt. Carbon-dioxide fluxes from a MORB-like source into the subcontinental lithospheric mantle along the East African Rift (5.31×10^9 mol/year; Lee et al., 2017) and of magmatic origin along rift faults at the Kenya Rift (300 kg/day; Robertson et al., 2016) further support this idea.

Studies of fluid inclusions indicate that the known widespread CO_2 emission from the asthenosphere at continental rifting is resulting from asthenosphere upwelling and its addition to the lithospheric mantle together with asthenospheric fluid-rich melt – lherzolite interaction (or autometasomatism), that leaves a CO_2-rich fluid behind. Such residual fluid can then be transferred from the upper mantle or lower crust along these deep faults, as suggested by Lee et al. (2016).

8. Conclusions

In this study, we examined fluid inclusions of asthenospheric origin, enclosed in deformed spinel lherzolites from Mt. Quincan, northeastern Queensland, Australia. The inclusions, entrapped along lamellae in pyroxene porphyroclasts, contain fluids composed of 75-89 mol % CO_2, 9-18 mol % H_2O, 0.1-1.7 mol % N_2 and ≤ 0.5 mol % H_2S, as well as dissolved trace elements. The CO_2-rich fluid phase can be interpreted as the residual fluid left behind after metasomatic enrichment of lherzolite in the spinel stability field beneath the area. The metasomatism resulted in the enrichment of LREE, Nb, Sr and Ti in clinopyroxene and the formation of pargasite in a small modal proportion (less than 1 %). Moreover, the abundance of pargasite also shows positive correlation with the abundance of fluid inclusions

Our findings suggest that the metasomatic agent was most likely a fluid phase with dissolved silicate melt from the asthenosphere. The driving force of the release of the fluid is likely associated with the thinning of the lithosphere by continental rifting. Upon following cooling, possibly due to the thermal relaxation of the isotherms and the upward migration of the fluid phase, the investigated lherzolites reached the pargasite stability conditions, which resulted in pargasite

formation. We conclude that pargasite, even if present only in very limited modal proportions, could be a common phase at spinel lherzolite stability conditions in the lithospheric upper mantle in continental rift-back arc settings.

Acknowledgements

The authors are grateful to Christina Günther and Andrea Perucchi for their assistance in electron microprobe analyses and synchrothron-radiated FTIR analyses, respectively. Gábor Varga and Ábel Szabó are also thanked for their help in FIB-SEM slicing. This work was supported by the Hungarian Scientific Research Fund (OTKA, project no. 105410) and a Bolyai Postdoctoral Fellowship Program grant awarded to M. Berkesi. We also thank for the support of "Grant-in-Aid of the Ministry of Education, Science, Sports and Culture (project no: 17684029 and 16GS021499)" and "The 21st Century Center of Excellence Program (Towards a new basic science; depth and synthesis)". Careful reviews of Tomo Morishita and Anastassia Borisova and the editorial handling of François Faure and Klaus Mezger helped to improve the paper. This is the 90th publication of the Lithosphere Fluid Research Lab.

References

Allen, C.M., Wooden, J.M. and Chappell, B.W. (1997). Late Paleozoic crustal history of central coastal Queensland interpreted from geochemistry of Mesozoic plutons: The effects of continental rifting. *Lithos*, **42**, 67-88.

Andersen, T., O'Reilly, S. Y. and W.L. Griffin, W.L. (1984). The trapped fluid phasein upper mantle xenoliths from Victoria, Australia: implications for mantle metasomatism. *Contrib. Mineral. Petrol.* **88**, 72-85.

Andersen, T. and Neumann, E. R. (2001). Fluid inclusions in mantle xenoliths. *Lithos* **55**, 301-320.

Anderson, A. and McCarron, T. (2011). Three-dimensional textural and chemical characterization of polyphase inclusions in spodumene using a dual focused ion beam-scanning electron microscope (FIB-SEM). *Can. Mineral.* **49**, 541–553.

Anders, E. and Grevesse, N. (1989). Abundances of the elements: meteoric and solar. *Geochim.Cosmochim. Acta* **53**, 197–214.

Arai, S. (1992). Chemistry of chromian spinel in volcanic rocks as a potential guide to magma chemistry. *Min. Mag.*, **56**, 173–184.

Arai, S. (1994). Characterization of spinel peridotites by olivine–spinel compositional relationships: review and interpretation. *Chem. Geol.*, 113, 191–204.

Ayers, J. (1998). Trace element modeling of aqueous fuid - peridotite interaction in the mantle wedge of subduction zones *Contrib. Mineral. Petrol. **132***, 390-404.

Bakker, R. J. (2003). Package FLUIDS 1. Computer programs for analysis of fluid data and for modelling bulk fluid properties, *Chem. Geol.*, **194**, 3-23.

Bedini, R. M., Bodinier, J. L., Dautria, J. M. and Morten, L. (1997). Evolution of LILE-enriched small melt fractions in the lithospheric mantle: a case study from the East African Rift. *Earth Planet. Sci. Lett.*, **153**, 67-83.

Berkesi, M., Guzmics, T., Szabó, C., Dubessy, J., Bodnar, R.J., Hidas, K. and Ratter, K. (2012). The role of CO_2-rich fluids in trace element transport and metasomatism in the lithospheric mantle beneath the Central Pannonian Basin, Hungary, based on fluid inclusions in mantle xenoliths. *Earth. Planet. Sci. Lett.* **331-332**, 8-20.

Berkesi, M., Káldos, R., Park, M., Szabó, C., Váczi, T., Török, K., Németh, B. and Czuppon, Gy. (2017). Detection of small amounts of N_2 in CO_2-rich high density fluid inclusions in mantle xenoliths, *Eur. J. Min.*, **3**, 423-431.

Borisova, A. Y., Ceuleneer, G., Kamenetsky, V. S., Arai, S., Béjina, F., Abily, B., Bindeman, I.N., Polvé, M., de Philippe, P., Aigouy, T. and Pokrovski, G.S. (2012). A NewView on the Petrogenesis of the Oman Ophiolite Chromitites from Microanalyses of Chromite-hosted Inclusions, *J. Petrology*, **53**, 2411-2440.

Brey, G. P., and T. P. Köhler (1990). Geothermobarometry in four phase lherzolites II.New thermobarometers and practical assessment of existing thermobarometers, *J. Petrology*, **31**, 1353-1378.

Czuppon, G., Matsumoto, T., Handler, M.R. and Matsuda, J. (2009). Noble gases in spinel peridotite xenoliths from Mt Quincan, North Queensland, Australia: Undisturbed MORB-type noble gases in the subcontinental lithospheric mantle. *Chem. Geol.*, **266**, 19–28.

Dawson, J.B. (1984). Contrasting types of upper-mantle metasomatism? Dev. Petrol, **11**, 289-294.

Della Ventura, G., Hawthorne, F.C., Robert, J-L. And Iezzi, G. (2003). Synthesis and infrared spectroscopy of amphiboles along the tremolite-pargasite join. *Eur. J. Min.*, **15,** 341-347.

Donchak P. J. T. (1997). Hodgkinson Province. In North Queensland Geology, Vol. 9 (eds. J. H. C. Bain and J. J. Draper). AGSO Bulletin 240/Queensland Department of Mines and Energy Geology.

Ewart A. (1982). Petrogenesis of the Tertiary anorogenic series of southern Queensland, Australia, in the light of trace element geochemistry and Sr and Pb isotopes, *J. Petrol.*, **23**, 344-382.

Falus, G., Szabó, C. and Vaselli, O (2000). Mantle upwelling within the Pannonian Basin: evidence from xenolith lithology and mineral chemistry, *Terra Nova*, **12**, 295-302.

Ferrando, S., Frezzotti, M. L., Neumann, E. R., De Astis, G., Peccerillo, A., Dereje, A., Gezahegn, Y. and Teklewold, A. (2008). Composition and thermal structure of the lithosphere beneath the Ethiopian plateau: evidence from mantle xenoliths in basanites, Injibara, Lake Tana Province. *Mineral. Petrol*. **93**, 47–78.

Fishwick, S., Heintz, M., Kennett, B. L. N., Reading, A. M. And Yoshizawa, K.. (2008). Steps in lithospheric thickness within eastern Australia, evidence from surface wave tomography. *Tectonics*, **27**, TC4009, doi:10.1029/2007TC002116

Frezzotti, M.L., Ferrando, S., Peccerillo, A., Petrelli, M., Francesca Tecce. F. and Perucchi, A. (2010). Chlorine-rich metasomatic H_2O–CO_2 fluids in amphibole-bearing peridotites from Injibara (Lake Tana region, Ethiopian plateau): nature and evolution of volatiles in the mantle of a region of continental flood basalts. *Geochim. Cosmochim. Acta* **74**, 3023–3039

Frezzotti, M. L., Tecce, F. and Casagli, A. (2012a). Raman spectroscopy for fluid inclusion analysis. *J. Geochem. Explor*., **112**, 1-20.

Frezzotti, M. L., Ferrando, S., Tecce, F. and Castelli, D. (2012b). Water content and nature of solutes in shallow-mantle fluids from fluid inclusions. *Earth Planet. Sci. Lett*., **351–352**, 70-83.

Frezzotti, M. L., and A. Peccerillo (2007). Diamond-bearing COHS fluids in the mantle beneath Hawaii, *Earth Planet. Sci. Lett*., **262**, 273–283.

Frezzotti, M.L. & Touret, J.L.R. (2014). CO_2, carbonate-rich melts, and brines in the mantle. *Geosci. Front*., **5**, 697–710.

Fumagalli, P., Zanchetta, S.and Poli, S. (2009). Alkali in phlogopite and amphibole and their effects on phase relations in metasomatized peridotites: a high-pressure study. *Contrib. Mineral. Petrol.* **158**, 723–737

Galvez, M. E., Connolly, J.A.D. and Manning, C.E. (2016). Implications for metal and volatile cycles from the pH of subduction zone fluids. *Nature Letter*, **539**, 420-425.

Gasparik, T. (2000). An Internally Consistent Thermodynamic Model for the System CaO-MgO-Al_2O3-SiO_2 Derived Primarily from Phase Equilibrium Data. *J. Geol.*, **108**, 103-119.

Gerya, T.V., Stöckhert, B. and Perchuk, A, L. (2002). Exhumation of high-pressure metamorphic rocks in a subduction channel: A numerical simulation. *Tectonics*, **21**, 1056, doi:10.1029/2002TC001406.

Green, T.H., Sie, S.H., Ryan, C.G. and Cousens, D.R. (1989). Proton microprobe-determined partitioning of Nb, Ta, Zr, Sr and Y between garnet, clinopyroxene and basaltic magma at high pressure and temperature. *Chem. Geol.* **74**, 201–216.

Green, D.H., Hibberson, W.O., Kovács, I. and Rosenthal, A. (2010). Water and its influence on the lithosphere-asthenosphere boundary. *Nature*, **467**(7314), p.448.

Green, D.H. (2015). Experimental petrology of peridotites, including effects of water and carbon on melting in the Earth's upper mantle. *Phys. Chem. Mineral*. **42**, 95–122

Griffin, W.L., Wass, S.Y. and Hollis, J.D. (1984) Ultramafic xenoliths from Bullenmerri and Gnotuk maars, Victoria, Australia: petrology of a sub-continental crust-mantle transition. *J. Petrol.* **25**, 53-87.

Griffin, W.L., Sutherland, F.L. and Hollis, J.D. (1987) Geothermal profile and crust/mantle transition beneath east/central Queensland: volcanology, xenolith petrography and seismic data. *J. Volc. Geotherm. Res.* **31**, 177-203.

Harte, B. (1983). Mantle peridotites and processes-the kimberlite sample. In: Hawkesworth, C.J., Norry, M.J. (eds) Continental basalts and mantle xenoliths. Shiva, Nantwich, pp. 46-91.

Handler, M.R., Bennett, V.C. and Carlson, R.W. (2005). Nd, Sr and Os isotope systematics in young, fertile peridotite xenoliths from northern Queensland, Australia: a unique view of depleted MORB mantle? *Geochim. Cosmochim. Acta* **69**, 5747–5763.

Hill D. (1951) Geology. In Handbook of Queensland, pp. 13–24. Australian and New Zealand Association for the Advancement of Science Report.

Huang, J-X., Gréau, Y., Griffin, W.L., O'Reilly S. Y. and Pearson, N. (2012). Multi-stage origin of Roberts Victor eclogites: Progressive metasomatism and its isotopic effects. *Lithos* **142-143**, 161-181.

Ingrin, J. and Skogby, H. (2000). Hydrogen in nominally anhydrous upper/mantle minerals: concentration levels and implications. *Eur. J. Mineral*. **12**, 543-570.

Ionov, D.A. and Hoffmann, A.W. (1995). Nb-Ta-rich mantle amphiboles and micas: Implications for subduction-related metasomatic trace element fractionations. *Earth. Planet. Sci. Lett.* **131**, 341-356.

Iwamori, H. (1998). Transportation of H_2O and melting in subduction zones, *Earth Planet. Sci. Let.* **160**, 65– 80.

Jenkins, D.M., Bozhilov, K.N. and Ishida, K. (2003). Infrared and TEM characterization of amphiboles synthesized near the tremolite-pargasite join in the ternary system tremolite-pargasite-cummingtonite. *Am. Mineral*., **88**, 1104–1114.

John, T., Gussone, N., Podladchikov, Y.Y., Bebout, G. E., Dohmen, R., Halama, R., Klemd, R., Magna, T and Seitz, H-M. (2012). Volcanic arcs fed by rapid pulsed fluid flow through subducting slabs. *Nature* **5**, 489-492.

Kang, P., Lamb, W.M. and Drury, M. (2017). Using mineral equilibria to estimate H_2O activities in peridotites from the Western Gneiss Region of Norway. *Am. Mineral.*, **102**, pp.1021-1036.

Kennett, B. L. N., Fishwick, S., Reading, A. M. and N. Rawlinson, N. (2004). Contrasts in mantle structure beneath Australia—Relation to Tasman Lines, *Aust. J. Earth Sci.* **51**, 563 – 569.

Keppler, H. (1996). Constraints from partitioning experiments on the composition of subduction zone fluids. *Nature* **380**, 237-240.

Kessel, R., Schmidt, M.W., Ulmer, P. and Pettke, T. (2005). Trace element signature of subduction-zone fluids, melts and supercritical liquids at 120–180 km depth. *Nature*, **437**, 724-727.

Kositcin, N., Champion, D. and Huston, D.L. (2009). Geodynamic synthesis of north Queensland region and implications for metallogeny. Geoscience Australia Record. 2009/30, p. 201.

Kovács, I., Green, D.H., Rosenthal, A., Hermann, J., O'neill, H.S.C., Hibberson, W.O. and Udvardi, B. (2012). An experimental study of water in nominally anhydrous minerals in the upper mantle near the water-saturated solidus. *J. Petrol.*, **53**, 2067-2093.

Kovács, I., Lenkey, L., Green, D.H., Fancsik, T., Falus, G., Kiss, J., Orosz, L., Angyal, J. and Vikor, Z. (2017). The role of pargasitic amphibole in the formation of major geophysical discontinuities in the shallow upper mantle. *Acta Geod. Geophys*, **52,** 183-204.

Lee, H., Muirhead, J.D., Fischer, T.P., Ebinger, C.J., Kattenhorn, S. A., Sharp, Z. D., Kianji, G., (2016). Massive and prolonged deep carbon emissions associated with continental rifting *Nature Geosci.* **9**, 145–149.

Lee, H., Fischer, T.P., Muirhead, J.D., Ebinger, C.J., Kattenhorn, S. A., Sharp, Z. D., Kianji, G., Takahata, N. and Sanof, Y. (2017). Incipient rifting accompanied by the release of subcontinental lithospheric mantle volatiles in the Magadi and Natron basin, East Africa. *J. Volcanol. Geotherm. Res.* **346**, 118-133.

Leisen, M., Dubessy, J., Boiron, M-C., Lach, P. (2012). Improvement of the determination of element concentrations in quartz-hosted fluid inclusions by LA-ICP-MS and Pitzer thermodynamic modeling of ice melting temperature. *Geochim. Cosmocim. Acta*. **90**, 110-125.

McDonough W. F. and Sun S. S. (1995). Composition of the earth. *Chem. Geol.* **120**, 223–253.

Manning C. E. (2004) The chemistry of subduction-zone fluids. *Earth Planet. Sci. Lett*. **223**, 1-16.

Mercier, J-C.C. and Nicholas, A. (1975). Textures and Fabrics of Upper-Mantle Peridotites as Illustrated by Xenoliths from Basalts. *J. Petrol*. **16**, 454-487.

Murgulov, V., Griffin, W. L., O'Reilly, S.Y. (2012). Temporal correlation of magmatic-tectonic events in the lower and upper crust in north-east Australia. *Int. J. Earth. Sci.* (Geol Rundsch) **101**, 1091–1109.

Nicholls, I.A. and Harris, K.L. (1979). Experimental rare earth element partition coefficients for garnet, clinopyroxene and amphibole coexisting with andesitic and basaltic liquids. *Geochim. Cosmochim. Acta* **44**, 287-308.

Niida, K., and Green, D.H. (1999) Stability and chemical composition of pargasitic amphibole in MORB pyrolite under upper mantle conditions. *Contrib. Mineral. Petrol*. **135**, 18–40.

O'Reilly, S.Y., and Griffin, W.L. (1988) Mantle metasomatism beneath Victoria, Australia: metasomatic processes in Cr-diopside lherzolites. *Geochim Cosmochim Acta* **52**, 433-447

O'Reilly S.Y., Griffin W.L. (2013) Mantle Metasomatism. In: Metasomatism and the Chemical Transformation of Rock. Lecture Notes in Earth System Sciences. Springer, Berlin, Heidelberg, doi: 10.1007/978-3-642-28394-9_12.

Park, M., Berkesi, M., Jung, H. and Kil, Y. (2017). Fluid infiltration in the lithospheric mantle beneath the Rio Grande Rift, USA: a fluid-inclusion study. *Eur. J. Mineral.*, **29**, 1-13.

Paton, C., Hellstrom, J., Paul, B.,Woodhead, J. and Hergt, J. (2011). Iolite: Freeware for the visualisation and processing of mass spectrometric data. *J. Anal. At. Spectrom.*, **26**, 2508-2518.

Peacock, S. M. (1990). Fluid Processes Subduction Zones. *Science* **248**, 329-337.

Peslier, A.H., Luhr, J.F. and Post, J. (2002). Low water contents in pyroxenes from spinel peridotites of the oxidized, sub-arc mantle wedge. Earth. Planet. Sci. Lett. **201**, 69-86.

Pintér, Z., Patkó, L., Tene Djoukam, J. F., Kovács, I., Tchouankoue, J. P., Falus, G., Konc, Z., Tommasi, A., Barou, F., Mihály, J., Németh, C. and Jeffries, T. (2015). Characterization of the sub-continental lithospheric mantle beneath the Cameroon volcanic line inferred from alkaline basalt hosted peridotite xenoliths from Barombi Mbo and Nyos Lakes. *J. Afr. Earth Sci.* **111**, 170-193.

Pironon, J., Grimmer, J. O.W., S. Teinturier, S., Guillaume, D. and Dubessy, J. (2003). Dissolved methane in water: temperature effect on Raman quantification in fluid inclusions, *J. Geochem. Exp*. **78-79**, 111-115.

Rey, P. (2001). From lithospheric thickening and divergent collapse to active continental rifting. In: Miller, J. A., Holdsworth, R. E., Buick, I. S. and Hand, M. (eds): Continental Reactivation and Reworking.Geological Society, London, Special Publications, 184, 77-88.

Robertson, E., Biggs, J., Edmonds, M., Clor, L., Fischer, T.P., Vye-Brown, C., Kianji, G., Koros, W. and Kandie, R. (2016). Diffuse degassing at Longonot volcano, Kenya: Implications for CO_2 flux in continental rifts. *J. Volcanol. Geotherm. Res.* **327**, 208–222.

Roedder, E. (1984), Fluid inclusions. *Rev. Mineral.* **12**, 1-646.

Rosso, K. M., and Bodnar, R.J. (1995). Microthermometric and Raman spectroscopic detection limits of CO_2 in fluid inclusions and the Raman spectroscopic characterization of CO_2. *Geochim Cosmochim. Acta* **59**, 3961-3975.

Scambelluri, M. and Philippot, P. (2001). Deep fluids in subduction zones, *Lithos* **55**, 213-227.

Scambelluri, M., Pettke, T. and Cannaòa, E. (2015). Fluid-related inclusions in Alpine high pressure peridotite reveal trace element recycling during subduction-zone dehydration of serpentinized mantle (Cima di Gagnone, Swiss Alps). *Earth. Planet. Sci. Lett.* **429**, 45–59.

Schellart, W.P., Lister, G.P. and Toy, V.G. (2006). A Late Cretaceous and Cenozoic reconstruction of the Southwest Pacific region: Tectonics controlled by subduction and slab rollback processes. *Earth. Sci. Rev*. **76**, 191–233.

Skogby, H. (2006). Water in natural mantle minerals I: pyroxenes. *Rev. Mineral Geochem.* **62**, 155-167.

Span, R., and Wagner, W. (1996). A new equation of state for carbon dioxide covering the fluid region from the triple-point temperature to 1100 K at pressures up to 800 MPa, *J. Phys. Chem. Ref. Data* **25**, 1513-1558.

Spandler, C., Pettke, T. and Rubatto, D. (2011). Internal and external fluid sources for eclogite-facies veins in the Monviso meta-ophiolite, Western Alps: implications for fluid flow in subduction zones. *J. Petrol.* **52**, 1207-1236.

Spengler, D., Obata, M., Hirajima, T., Ottolini, L., Ohfuji, H., Tamura, A. and Arai, S. (2012): Exsolution of garnet and clinopyroxene from high-Al pyroxenes in Xugou peridotite, Eastern China. *J. Petrol.* **53**, 1477-1504.

Stephenson, P.J. (1989). Northern Queensland. In: Johnson, R.W. (Ed.), Intraplate Volcanism in Eastern Australia and New Zealand. Cambridge University Press, Cambridge, pp. 89–97.

Sundvall, R. and Stalder, R. (2011). Water in upper mantle pyroxene megacrysts and xenocrysts: A survey study. *Am. Mineral*. **96**, 1215-1227.

Touret, J. L. R. (2001). Fluids in metamorphic rocks. In Fluid Inclusions: Phase Relationships – Methods – Applications, vol. 55 (eds. T. Andersen, M. L. Frezzotti and E. Burke). *Lithos,* **55,** 1–27.

Tumiati, S., Tiraboschi, C., Sverjensky, D.A., Pettke, T., Recchia, S., Ulmer, P., Miozzi, F. and. Poli, S. (2017). Silicate dissolution boosts the CO_2 concentrations in subduction fluids. Nature **8**, doi:10.1038/s41467-017-00562-z.

Viti C. and Frezzotti M. L. (2000) Re-equilibration of glass and CO_2 inclusions in xenolith olivine: a TEM study. *Am. Mineral.* **85**, 1390–1396.

Wendlandt RF, Harrison WJ (1979) Rare earth partitioning between immiscible carbonate and silicate liquids and CO_2 vapor: results and implications for the formation of light rare earth-enriched rocks. Contrib. Mineral. Petrol. **69**, 409-419

Young, H. P. and Lee, C.-T.A. (2009). Fluid-metasomatized mantle beneath the Ouachita belt of southern Laurentia: Fate of lithospheric mantle in a continental orogenic belt. *Lithosphere,* **1**, 370-383.

Zhang, M., Stephenson, P.J., O'Reilly, S.Y., McCulloch, M.T. and Norman, T. (2001). Petrogenesis and Geodynamic Implications of Late Cenozoic Basalts in North Queensland, Australia: Trace-element and Sr–Nd–Pb Isotope Evidence. *J. Petrol.* **42**, 685-719.

Zorin, Y. A. and Lepina, S. V. (1985). Geothermal aspects of development of astheospheric upwellings beneath continental rift zones. *J. Geodyn*. **3**, 1-22.

Figure caption

Figure 1.

Photomicrographs of the studied rock and their fluid inclusions A) Porphyroclastic textured spinel lherzolite (JMTQ20) with orthopyroxene porphyroclasts (framed) and small neoblasts. Plane polarized light, transmitted light B) Close-up view of area marked by the frame on the right on Fig 1A, highlighting the relationship of fine exsolution lamellae and fluid inclusions in the orthopyroxene porphyroclasts. Plane polarized light, transmitted light C) Back-scattered electron image of an orthopyroxene porphyroclast (left frame on Fig 1A) and its enclosed clinopyroxene (cpx) and spinel (spl) lamellae D) Back-scattered electron image of pargasite (prg) in clinopyroxene (cpx) associated with spinel (spl) and orthopyroxene in JMTQ20 spinel lherzolite. E) High magnification plane polarized light image of fluid inclusions with liquid (L) and solid (S) phases in JMTQ45 spinel lherzolite. F) High magnification plane polarized light image of fluid inclusions (indicated by the arrows) and their association with the lamellae (dashed curve) in orthopyroxene from the sample JMTQ20.

Figure 2

Mg# (100*Mg/(Mg+Fe)) in olivine versus Cr# (100*Cr/(Cr+Al)) of coexisting spinel in the studied Mt. Quincan xenoliths. The two thick curves mark the Olivine-Spinel Mantle Array (OSMA) determined by Arai et al., (1994). FMM-Fertile MORB Mantle composition and partial melting trends are from Arai (1992).

Figure 3

Trace element compositions of the studied spinel lherzolite xenoliths from Mt. Quincan. A) Primitive mantle-normalized (McDonough and Sun, 1995) trace element pattern of clinopyroxenes. Curves denote average data of each element; error bars show the standard deviations. The difference from the fluid inclusion-free (JMTQ11) through the fluid inclusion-bearing (JMTQ45) to the fluid inclusion-rich (JMTQ20) xenolith is well observable in their LREE, Sr, Nb and Ti contents. B) Amphibole/clinopyroxene element ratios in JMTQ20 fluid-inclusion rich spinel lherzolite. The ratio plots around 1 for the majority of the elements, except for Rb, Ba, Nb, Sr and Ti. C) Chondrite-normalized (Anders and Grevesse, 1989) rare earth element (REE) patterns of the studied xenoliths. In the fluid inclusion-bearing (JMTQ45) and fluid inclusion-rich (JMTQ20) xenoliths, pargasite REE pattern is shown as well. Calculated melt composition (referred to as calc.melt), taking into account the pargasite/basaltic melt partition coefficient (using K_D Nicholls and Harris, 1979), compared with alkali basaltic composition from the studied area (referred to as AB, data from Zhang et al., 2001) is also shown.

Figure 4

Representative Raman spectra of the liquid phase, taken at room temperature in the spectral region of 2270-2350 cm^{-1} (A) and 2500-2700 cm^{-1} (B), showing the presence of small amount of N_2 (Raman band at ~2327 cm^{-1}) and H_2S (Raman band at ~2608 cm^{-1}) in CO_2-rich fluid inclusions. For more details about the detection of N_2, see Berkesi et al., 2017.

Figure 5

Raman spectra in the range of 2650-3950 cm^{-1} taken at different temperatures on the same fluid inclusion in xenolith JMTQ45. The corresponding temperatures are indicated on the right side of the spectra. Besides liquid H_2O (broad band between 3000 and 3700 cm^{-1}), the peak of dissolved H_2O in the CO_2-rich phase was also detected at room temperature. Upon heating, the band of liquid H_2O gradually disappears, while the peak of the dissolved H_2O increases. Total homogenization was determined at the point where the peak area of the dissolved H_2O stopped increasing despite further heating. The peak position of the dissolved H_2O was the same at each temperature. Peak positions (numbers above or below the peaks) were determined by fitting the peaks with Gaussian-Lorentzian sum profiles.

Figure 6

Representative example for the variation of the CO_2/H_2O Raman peak area as a function of temperature in a fluid inclusion from xenolith JMTQ20. During heating, the ratio decreased as a result of continuous dissolution. The minimum temperature at which the ratio reached a constant value was considered as the maximum temperature of total homogenization (abbreviated as T_{hom}^{total}).

Figure 7

Secondary electron images of exposed inclusions taken during focused ion beam (FIB) analyses in clinopyroxene- (A) and orthopyroxene- (B) hosted fluid inclusion. Solid phases within the

cavity of inclusions were previously identified as pargasite (Prg), magnesite (Mgs) and quartz (Qtz) by point measurements of Raman spectroscopy. Dashed lines mark the Raman spectrum of the host mineral, obtained in the same focal depth and with the same acquisition parameters as the solid phases in the inclusions. Asterisks denote the Raman bands of the host minerals.

Figure 8

(A) Photomicrograph of the area analyzed by FTIR for hyperspectral images, including a fluid inclusion (FI) in orthopyroxene (Opx). 1N, transmitted light. (B)-(D) Hyperspectral images showing the distribution of pargasite (Prg) (B), CO_2 (C) and H_2O liquid (D) in the FI and its host orthopyroxene. All images were obtained using a synchrotron source. (E) Characteristic IR spectra of the host orthopyroxene in the JMTQ20 spinel lherzolite, along with the IR bands of pargasite.

Figure 9

(A) Backscattered electron image and (B) EDS spectrum of a Fe-bearing sulfide daughter phase at the wall of an inclusion (JMTQ20). Note that the increasing intensity of Ga on the spectrum is a result of milling with the use of Ga^+-ions of the FIB-SEM instrument.

Figure 10

Representative LA–ICP-MS intensity versus time signals during ablation of an orthopyroxene-hosted fluid inclusion. The part of the spectrum labeled as ‘FI signal’ represents a mixed signal from both the host orthopyroxene and the fluid inclusion. In contrast, the part labeled as ‘host signal’ represents signal collected exclusively from the host orthopyroxene.

Figure 11

Pressure (GPa) − Temperature (°C) diagram showing the possible P-T ranges for lamellae along with pargasite formation and the entrapment of fluid inclusions. Spinel lhz/Garnet lhz reaction curves are from Niida and Green (1999). The grey line indicates the pargasite stability curve (dehydration solidus) in a model MORB pyrolite (MPY) after Niida and Green, 1999. Eastern Australian geotherm is after Griffin et al., (1987). "Paleo"-temperatures of the xenoliths are shown as open circles, whereas "neo"-temperatures are plotted with filled circles. Paleo- and neo-temperatures stand for the possible pressure and temperature range of a high-temperature opx before and after lamellae formation, respectively. MOHO depth position of the region is an approximated after Griffin et al., 1987; Mathur, 1983 and Clitheroe et al., 2000. LAB defines the lithosphere-asthenosphere boundary based on Fishwick et al. (2008). Symbols are the same as on Fig. 3. For further details, see text.

Figure 12

Schematic cross section for the crust-lithosphere-upper asthenosphere beneath the studied region (Mt. Quincan, northeastern Australia) explaining the metasomatism and entrapment of a fluid-rich melt. A) Continental rifting results in thinning of the lithosphere and shifting of the isotherms (dotted lines) while a fluid-rich melt or incipient melt is present in the mantle. At this state, the pargasite stability (dashed line) falls within the asthenosphere, thus pargasite cannot form. B) Post-extensional thermal relaxation results in cooling and thickening of the lithosphere. The isotherms

enter the pargasite stability field, thus the fluid-rich melt forms pargasite during interaction with the lherzolitic environment. Abbreviation: LAB – lithosphere-asthenosphere boundary.

Table 1 Major element composition (wt.% average) of constituent minerals of the Mt. Quincan xenoliths. Abbreviations: Cpx - clinopyroxene; Spl - spinel; n - number of analysis, s.d.-standard deviation.

	JMTQ11							
	spinel lherzolite - fluid inclusion free							
mineral phase	***Ol***		***Opx***		***Cpx***		***Spl***	
n	*8*		*17*		*15*		*7*	
	average	*s.d.*	*average*	*s.d.*	*average*	*s.d.*	*average*	*s.d.*
SiO_2	40.6	0.06	55.0	0.63	52.3	0.45	0.13	0.08
TiO_2	0.01	0.01	0.07	0.01	0.37	0.04	0.14	0.02
Al_2O_3	0.02	0.01	4.14	0.51	5.43	0.35	56.5	1.36
Cr_2O_3	0.01	0.01	0.31	0.08	0.36	0.05	10.7	1.12
FeO^{ta}	10.6	0.08	6.8	0.23	2.8	0.29	11.7	0.31
MnO	0.14	0.01	0.14	0.02	0.14	0.03	0.09	0.02
NiO	0.42	0.02	0.10	0.03	0.05	0.02	0.4	0.03
MgO	49.0	0.21	33.6	0.28	16.2	0.45	20.4	0.17
CaO	0.08	0.03	0.52	0.18	21.5	0.55	0.01	0.01
Na_2O	0.01	0.01	0.06	0.03	1.11	0.09	0.01	0.01
K_2O	0.00	0.00	0.00	0.00	0.00	0.00	0.00	0.00
Total	101.0	0.25	100.7	0.39	100.3	0.37	100.1	0.22
mg#[b]	0.89	0.00	0.90	0.00	0.90	0.01	0.76	0.01
cr#[c]							0.11	0.01
	JMTQ45							
	spinel lherzolite - fluid inclusion bearing							
mineral phase	***Ol***		***Opx***		***Cpx***		***Spl***	
n	*11*		*15*		*12*		*5*	
	average	*s.d.*	*average*	*s.d.*	*average*	*s.d.*	*average*	*s.d.*
SiO_2	40.7	0.12	54.8	0.3	51.7	0.20	0.04	0.02
TiO_2	0.01	0.01	0.09	0.02	0.35	0.04	0.11	0.02
Al_2O_3	0.02	0.01	4.76	0.21	6.50	0.16	55.9	0.77
Cr_2O_3	0.02	0.02	0.38	0.04	0.78	0.06	11.4	0.77
FeO^{ta}	9.73	0.09	6.41	0.08	3.21	0.11	12.0	0.17
MnO	0.13	0.01	0.14	0.01	0.09	0.02	0.10	0.01
NiO	0.39	0.02	0.1	0.02	0.05	0.02	0.41	0.02
MgO	49.1	0.14	32.5	0.18	16.3	0.10	20.6	0.17

CaO	0.06	0.00	0.81	0.05	20.8	0.32	0.01	0.00
Na_2O	0.01	0.01	0.06	0.02	1.09	0.04	0.01	0.00
K_2O	0.00	0.00	0.00	0.00	0.00	0.00	0.00	0.00
Total	100.2	0.22	100.0	0.4	100.8	0.38	100.6	0.27
mg#[b]	0.90	0.00	0.90	0.00	0.90	0.00	0.75	0.00
cr#[c]							0.12	0.01

	JMTQ20									
	spinel lherzolite-fluid inclusion rich									
mineral phase	***Ol***		***Opx***		***Cpx***		***Spl***		***Prg***	
n	*10*		*17*		*18*		*7*		4	
	average	*s.d.*	*average*	*s.d.*	*average*	*s.d.*	*average*	*s.d.*	*average*	*s.d.*
SiO_2	41.0	0.11	54.4	0.4	51.4	0.26	0.05	0.01	43.4	0.17
TiO_2	0.03	0.01	0.12	0.02	0.43	0.05	0.18	0.03	1.40	0.05
Al_2O_3	0.01	0.01	5.15	0.23	6.73	0.18	55.0	0.31	15.7	0.09
Cr_2O_3	0.02	0.01	0.40	0.04	0.73	0.06	11.4	0.49	1.03	0.08
FeO[a]	11.2	0.36	7.13	0.19	3.56	0.10	13.6	0.67	4.56	0.14
MnO	0.15	0.01	0.15	0.02	0.10	0.02	0.12	0.01	0.06	0.02
NiO	0.39	0.02	0.1	0.02	0.06	0.02	0.40	0.01	0.12	0.02
MgO	48.6	0.29	31.74	0.21	16.1	0.18	19.7	0.53	17.9	0.15
CaO	0.08	0.01	0.87	0.05	20.8	0.26	0.02	0.03	11.0	0.05
Na_2O	0.01	0.01	0.07	0.02	1.00	0.04	0.01	0.01	3.24	0.08
K_2O	0.00	0.01	0.00	0.00	0.00	0.01	0.01	0.00	0.31	0.03
Cl_2O									≤ 0.02	
Total	101.4	0.18	100.1	0.5	101.0	0.41	100.6	0.40	98.7	0.21
mg#[b]	0.89	0.00	0.89	0.00	0.89	0.00	0.72	0.01	0.90	0.02
cr#[c]							0.12	0.00		

[a] Total FeO given in Fe^{2+}.

[b] mg#=100×Mg/(Mg+Fe).

[c] cr#=100×Cr/(Cr+Al).

Table 2 Trace element composition of clinopyroxenes (Cpx) and pargasie (Prg /only in JMTQ20) of the Mt. Quincan xenolites (averages, in ppm). S.d. - standard deviation; n.d - not detected; n.a - not analyzed, n-number of measurement

	JMTQ11				**JMTQ45**				**JMTQ20**					
	Cpx (n=12)		Opx (n=10)		Cpx (n=11)		Opx (n=10)		Cpx (n=10)		Prg (n=5)		Opx (n=10)	
	average	*s.d.*	*average*	*s.d.*	*average*	*s.d.*	*average*	*s.d.*	*average*	*s.d.*	*average*	*s.d.*	*average*	*s.d.*
Rb	0.10	0.05	n.d.		0.19	0.02	0.14	0.11	0.08	0.07	3.87	1.15	0.07	0.00
Th	0.03	0.02	0.02	0.02	0.27	0.05	0.03	0.02	0.07	0.04	0.08	0.02	0.06	0.01
U	0.01	0.00	0.00	0.00	0.07	0.02	0.02	0.01	0.04	0.03	0.04	0.03	0.03	0.02
Ba	0.07	0.03	0.08	0.08	0.11	0.08	0.08	0.07	0.10	0.05	36.58	9.47	0.09	0.07
Nb	0.01	0.01	0.01	0.01	0.02	0.01	0.01	0.01	0.21	0.04	12.92	1.35	0.02	0.01
La	0.02	0.00	0.01	0.01	0.45	0.36	0.02	0.01	2.27	0.16	2.75	0.45	0.02	0.01
Ce	0.06	0.03	0.01	0.01	0.56	0.27	0.02	0.01	6.43	0.26	7.22	0.43	0.03	0.04
Pb	0.05	0.03	0.07	0.04	0.11	0.05	0.05	0.03	0.10	0.04	0.35	0.00	0.06	0.04
Pr	0.04	0.02	0.01	0.01	0.15	0.03	0.02	0.01	0.95	0.09	1.11	0.12	0.02	0.01
Sr	n.a.	n.a.	n.d.		12.10	1.80	n.d.		69.10	2.35	211.80	23.15	0.20	0.08
Nd	0.69	0.21	0.06	0.05	1.43	0.22	0.03	0.03	4.96	0.65	5.46	0.94	0.07	0.05
Zr	3.64	0.27	0.18	0.10	8.42	0.48	0.53	0.06	20.13	2.47	16.27	0.68	1.48	0.20
Sm	0.70	0.08	0.07	0.08	0.76	0.28	0.19	0.11	1.30	0.22	1.71	0.33	0.08	0.09
Eu	0.29	0.07	0.02	0.00	0.39	0.05	n.d.	n.d.	0.72	0.06	0.81	0.18	0.04	0.01
Ti	1845.7	162.6	407.9	74.89	1567.5	58.86	438.6	45.29	2220.9	227.8	10186.6	1323.3	602.0	55.04
Gd	1.28	0.21	0.11	0.10	1.46	0.55	0.11	0.06	2.10	0.40	2.48	0.37	0.12	0.09
Tb	0.29	0.05	0.01	0.01	0.29	0.11	0.01	0.01	0.39	0.03	0.44	0.05	0.01	0.01
Dy	2.08	0.25	0.05	0.04	2.27	0.09	0.09	0.05	2.67	0.15	3.11	0.38	0.14	0.10
Y	12.65	0.60	0.61	0.16	12.15	4.31	0.87	0.07	14.97	0.70	19.47	1.70	1.05	0.09
Ho	0.51	0.04	0.03	0.02	0.52	0.05	0.03	0.02	0.58	0.06	0.71	0.08	0.05	0.01
Er	1.49	0.19	0.07	0.05	1.35	0.48	0.11	0.06	1.53	0.14	2.11	0.18	0.12	0.07
Tm	0.20	0.02	0.02	0.01	0.18	0.06	0.03	0.02	0.22	0.03	0.28	0.05	0.04	0.01
Yb	1.38	0.23	0.20	0.09	1.27	0.44	0.19	0.07	1.46	0.19	2.00	0.37	0.26	0.07
Lu	0.19	0.04	0.03	0.01	0.17	0.06	0.04	0.02	0.21	0.02	0.24	0.06	0.04	0.02
Cr	4248.4	807.8	1941.5	544.6	4600.7	601.3	2340.4	275.8	4394.5	262.0	7979.7	482.1	2388.5	199.7
La_N/Lu_N	0.001	0.02	0.03	0.01	0.28	0.61	0.04	0.07	1.15	1.13	1.19	0.73	0.01	0.02

Table 3 Main results on fluid inclusions and their estimated composition of entrapment (in COHNS system, dissolved trace elements not included

Sample	Classification	Microthermometry		Raman spectroscopy	FIB-SEM	Estimated composition
		Tm	Th /density	fluid phase composition*	solid phases**	
		°C	*°C / g*cm^{-3}*	*mol%*	*vol%*	*mol%*
JMTQ45	fluid inclusion-bearing	-57.4 - -56.8	- 34.2 - -5.1 / 1.09 - 0.96	CO_2: 93.2-94.9, H_2O: 3.2-5.2, N_2: 0.3-2.1 , H_2S: ≤0.5	Mgs: 3.7-4.8, Qtz: 2.0-2.8, Prg: 13.0-15.3,	CO_2: 75-86, H_2O: 9-14, N_2: 0.1-1.7 and H_2S: ≤ 0.5
JMTQ20	fluid inclusion-rich	-57.5 - -56.5	- 35.2 - -8.9 / 1.10 - 0.98	CO_2: 93.8-94.6, H_2O: 4.1-5.9, N_2: 0.2-1.8 , H_2S: ≤0.5	Mgs: 3.1-5.2, Qtz: 2.6-3.3, Prg: 12.7-16.0, Fe-Ni sulfide: 0.7 vol%	CO_2: 79-89 mol%, H_2O: 11-18 mol%, N_2: 0.2-1.5 mol% and H_2S: ≤ 0.5 mol%

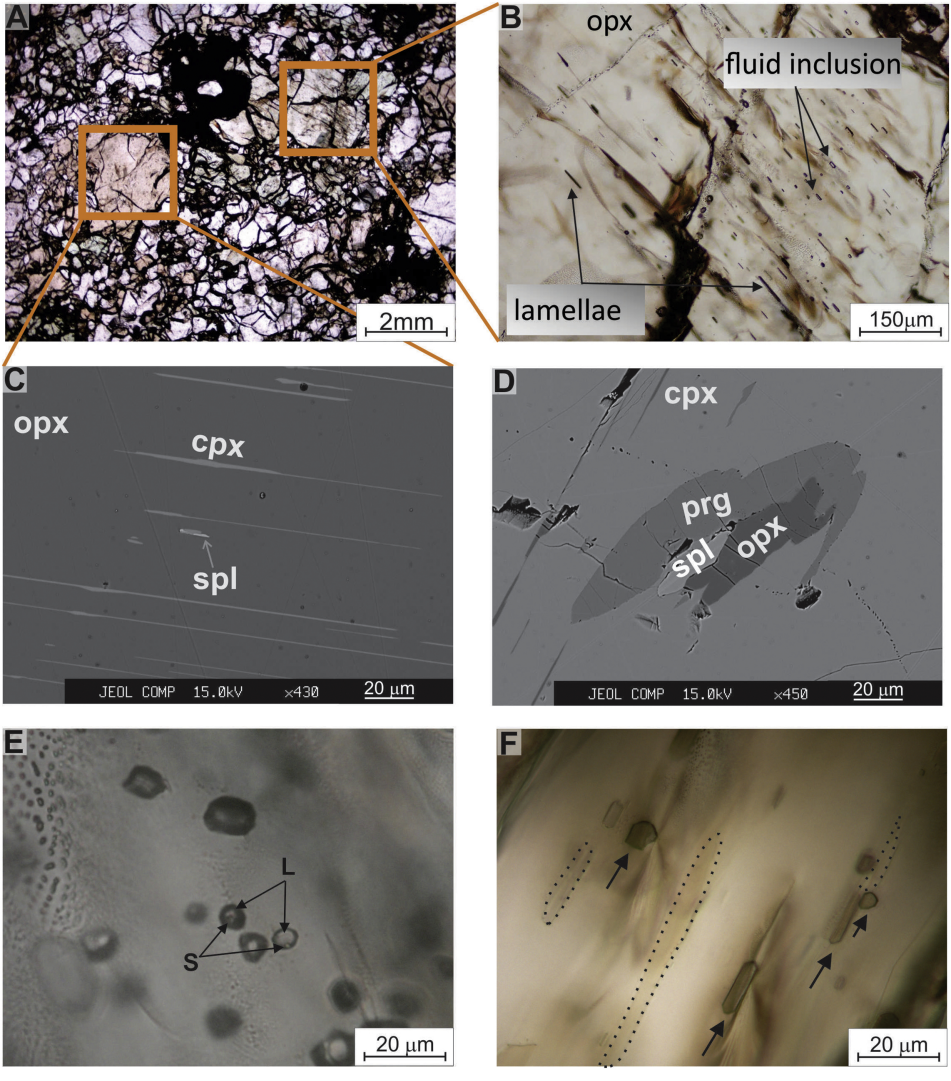
A
2mm
B
opx
fluid inclusion
lamellae
150µm
C
opx
cpx
spl
JEOL COMP 15.0kV ×430 20 µm
D
cpx
prg
spl
opx
JEOL COMP 15.0kV ×450 20 µm
E
L
S
20 µm
F
20 µm

Figure 1

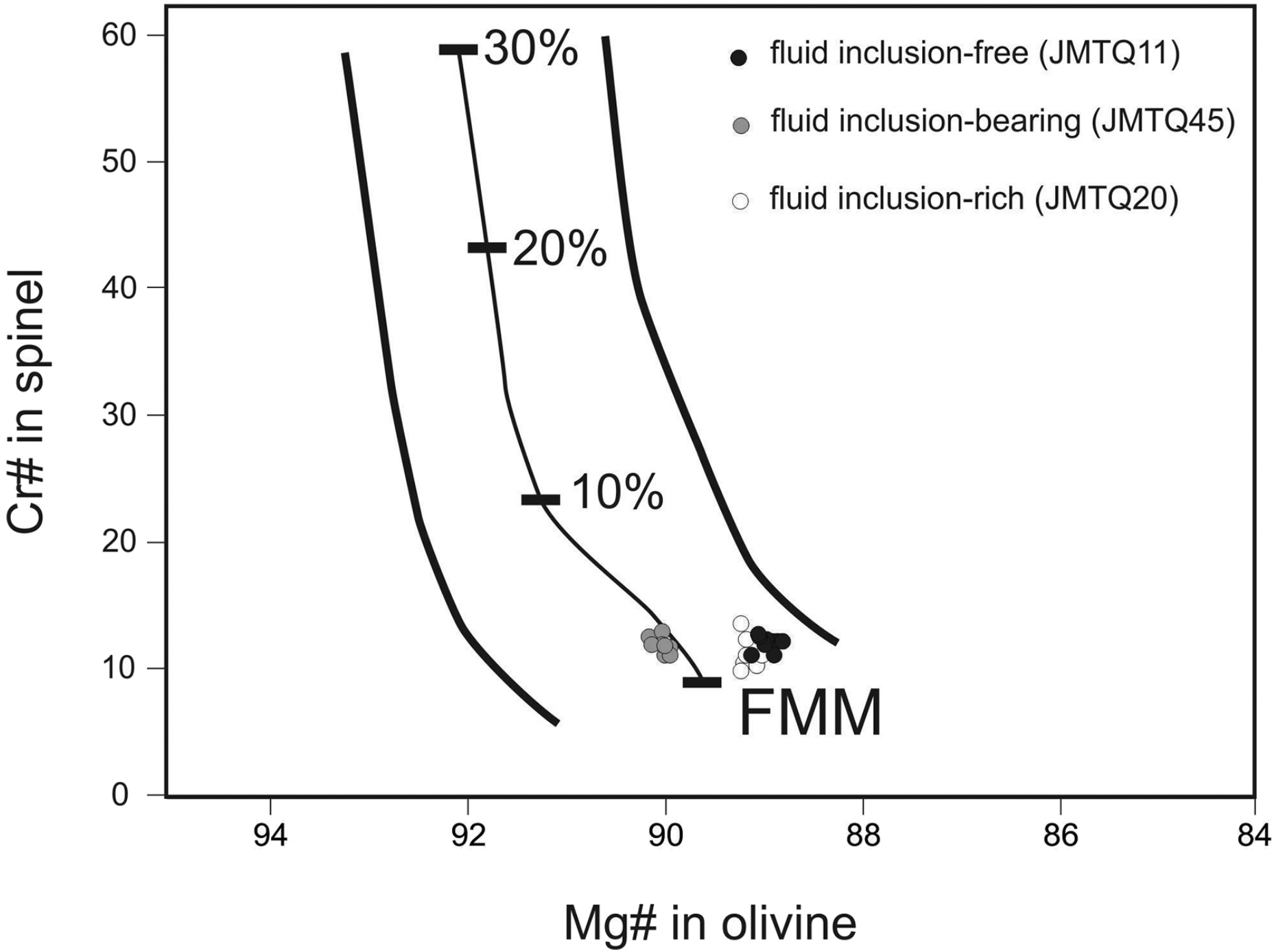
60
50
40
30
20
10
0
Cr# in spinel
30%
20%
10%
FMM
fluid inclusion-free (JMTQ11)
fluid inclusion-bearing (JMTQ45)
fluid inclusion-rich (JMTQ20)
94
92
90
88
86
84
Mg# in olivine

Figure 2

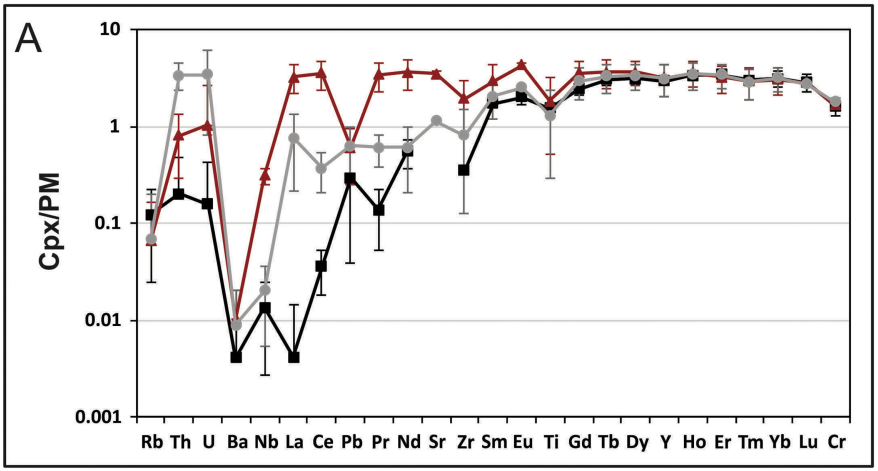
A
Cpx/PM
10
1
0.1
0.01
0.001
Rb Th U Ba Nb La Ce Pb Pr Nd Sr Zr Sm Eu Ti Gd Tb Dy Y Ho Er Tm Yb Lu Cr

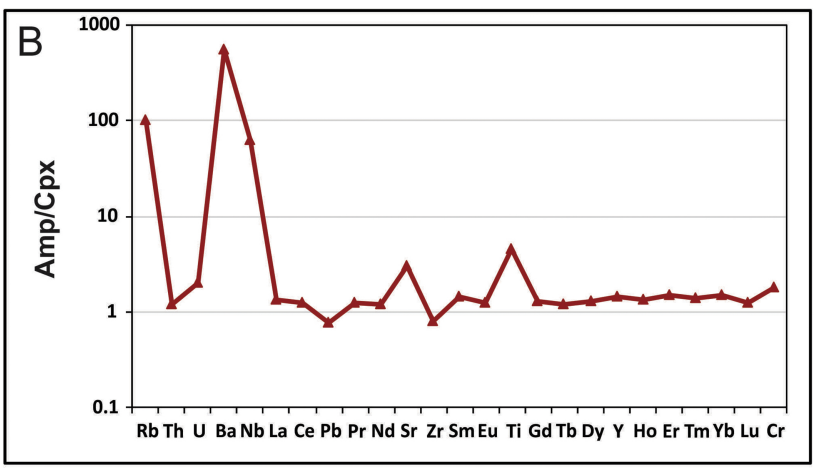
B
Amp/Cpx
1000
100
10
1
0.1
Rb Th U Ba Nb La Ce Pb Pr Nd Sr Zr Sm Eu Ti Gd Tb Dy Y Ho Er Tm Yb Lu Cr

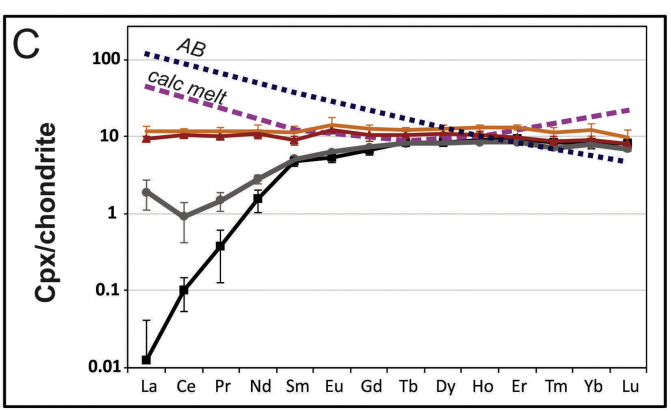
C
Cpx/chondrite
AB
calc melt
100
10
1
0.1
0.01
La Ce Pr Nd Sm Eu Gd Tb Dy Ho Er Tm Yb Lu
Legend:
Fl-free cpx
Fl-bearing cpx
Fl-rich cpx
Fl-rich amp

Figure 3

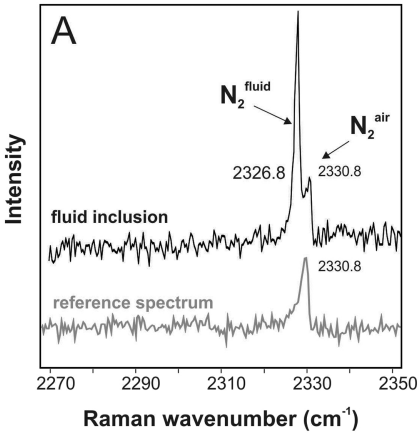
A
N_2^{fluid}
N_2^{air}
2326.8
2330.8
fluid inclusion
2330.8
reference spectrum
Intensity
2270
2290
2310
2330
2350
Raman wavenumber (cm^{-1})

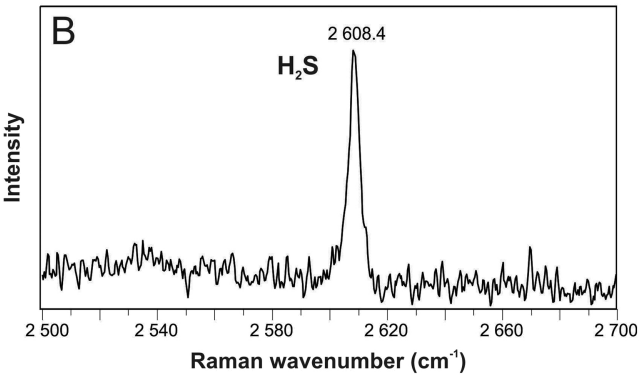
B
2 608.4
H_2S
Intensity
2 500
2 540
2 580
2 620
2 660
2 700
Raman wavenumber (cm^{-1})

Figure 4

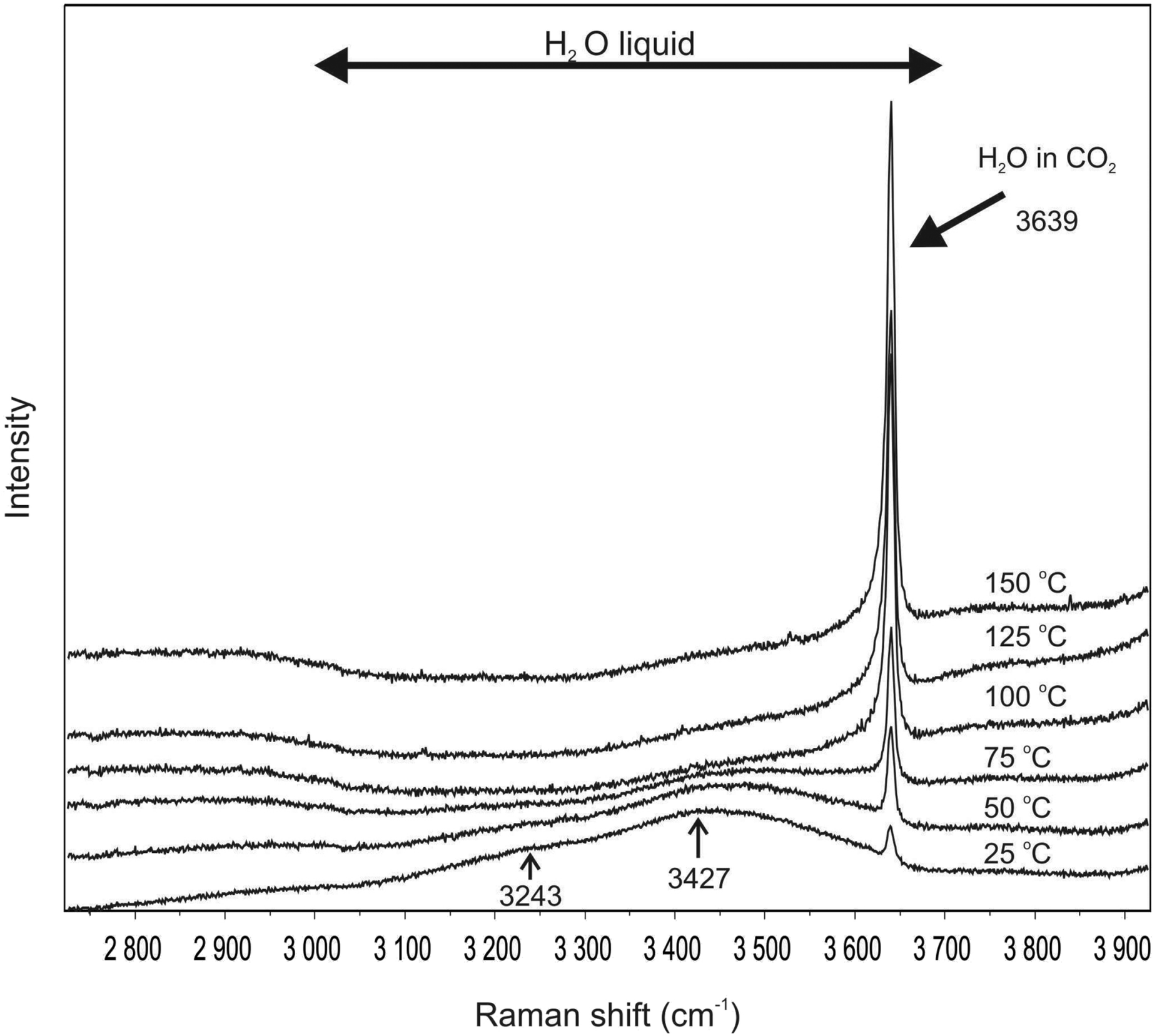
H2 O liquid
H2O in CO2
3639
150 °C
125 °C
100 °C
75 °C
50 °C
25 °C
3243
3427
Intensity
2 800
2 900
3 000
3 100
3 200
3 300
3 400
3 500
3 600
3 700
3 800
3 900
Raman shift (cm-1)

Figure 5

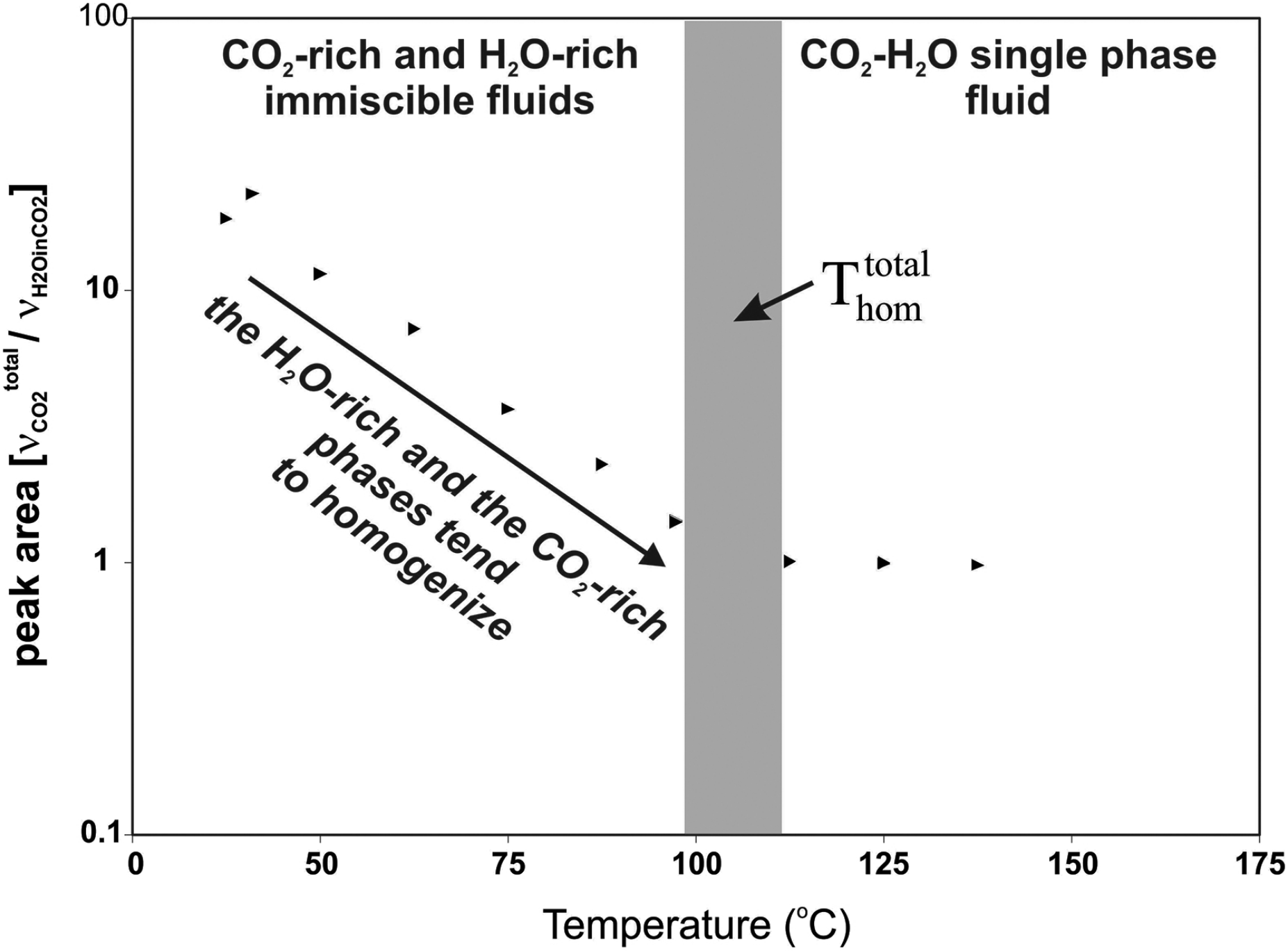
100
10
1
0.1
peak area [ν_{CO2}^{total} / $\nu_{H2OinCO2}$]
CO_2-rich and H_2O-rich immiscible fluids
CO_2-H_2O single phase fluid
T_{hom}^{total}
the H_2O-rich and the CO_2-rich phases tend to homogenize
0
50
75
100
125
150
175
Temperature (°C)

Figure 6

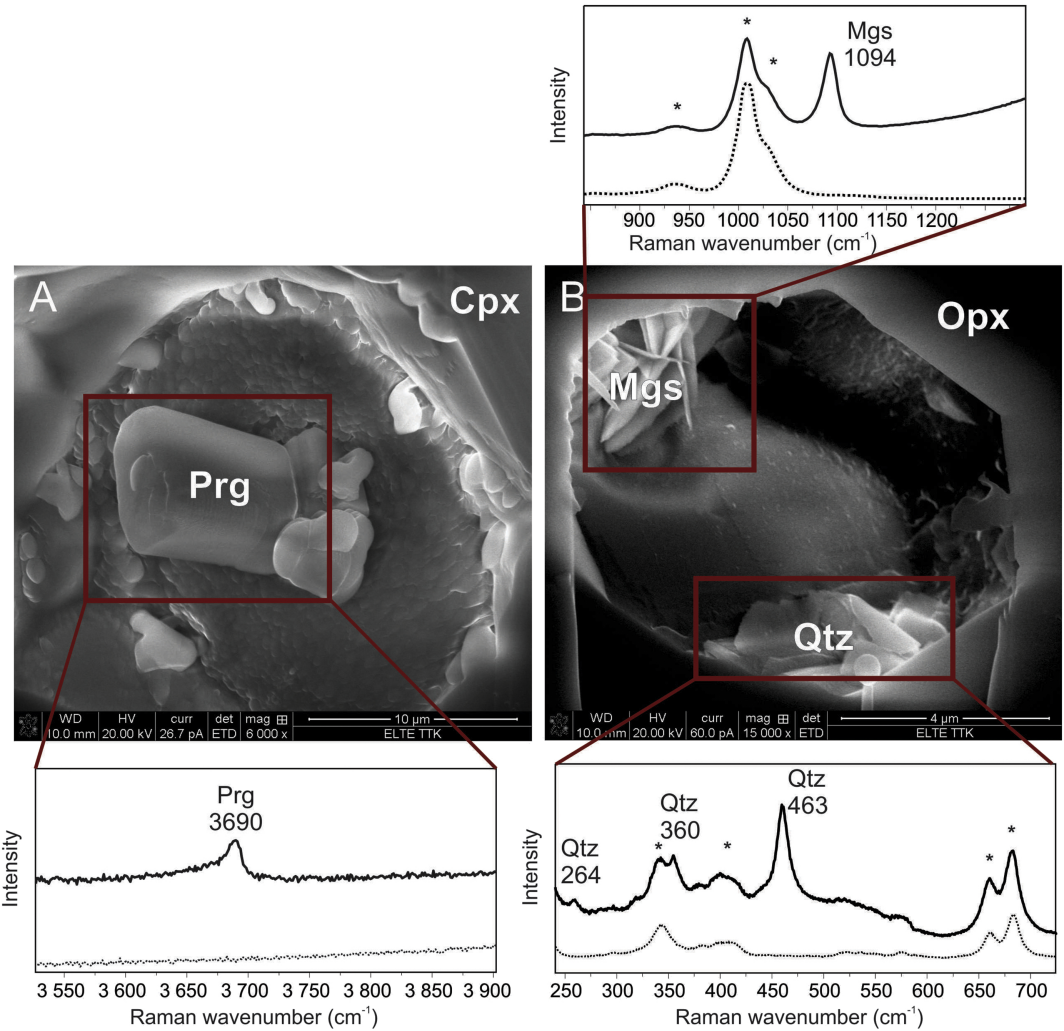
Mgs
1094
Intensity
900 950 1000 1050 1100 1150 1200
Raman wavenumber (cm-1)
A
Cpx
Prg
WD 10.0 mm | HV 20.00 kV | curr 26.7 pA | det ETD | mag 6 000 x | 10 µm | ELTE TTK
B
Opx
Mgs
Qtz
WD 10.0 mm | HV 20.00 kV | curr 60.0 pA | mag 15 000 x | det ETD | 4 µm | ELTE TTK
Prg
3690
Intensity
3 550 3 600 3 650 3 700 3 750 3 800 3 850 3 900
Raman wavenumber (cm-1)
Qtz
264
Qtz
360
Qtz
463
Intensity
250 300 350 400 450 500 550 600 650 700
Raman wavenumber (cm-1)

Figure 7

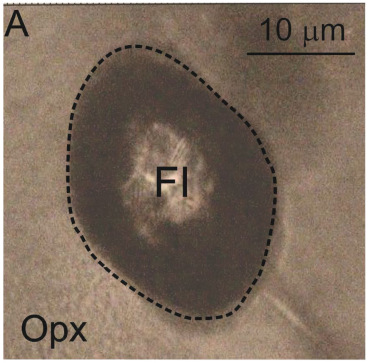

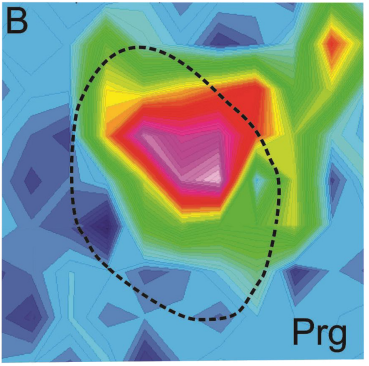

Relative concentration scale

higher

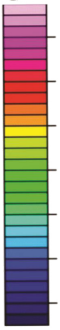

lower

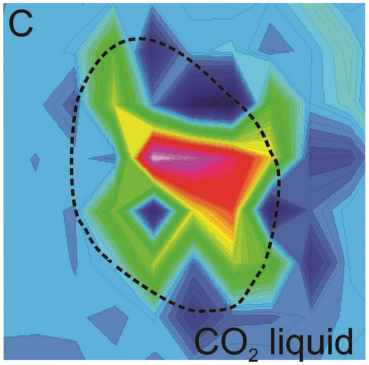

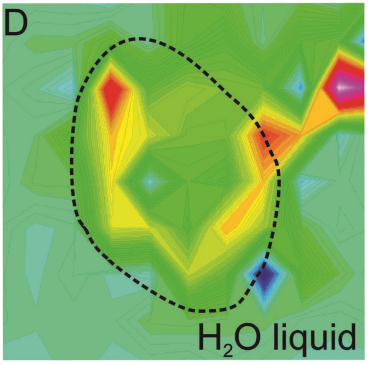

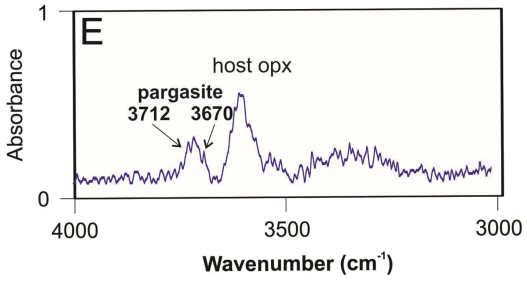

Figure 8

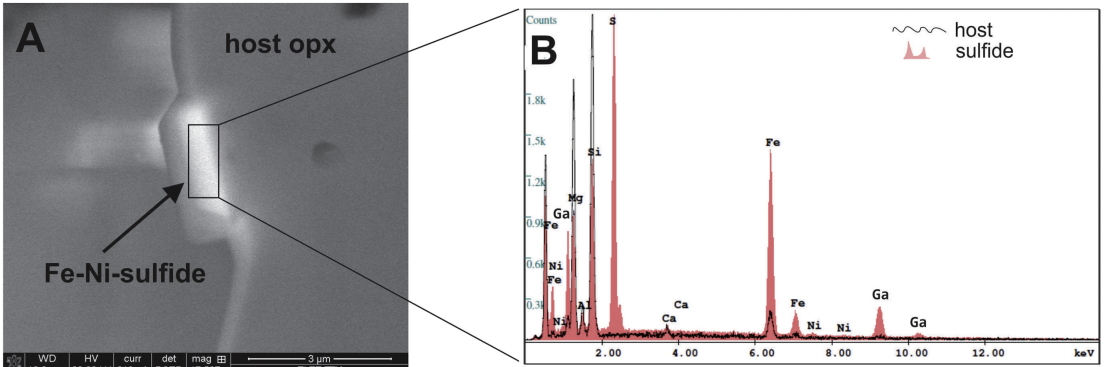
A
host opx
Fe-Ni-sulfide
WD 10.0 mm
HV 20.00 kV
curr 213 pA
det BSED
mag 17 527 x
3 µm
ELTE TTK
B
Counts
host
sulfide
S
Si
Fe
Mg
Ga
Fe
Ni
Fe
Ni
Al
Ca
Ca
Fe
Ni
Ni
Ga
Ga
1.8k
1.5k
1.2k
0.9k
0.6k
0.3k
2.00
4.00
6.00
8.00
10.00
12.00
keV

Figure 9

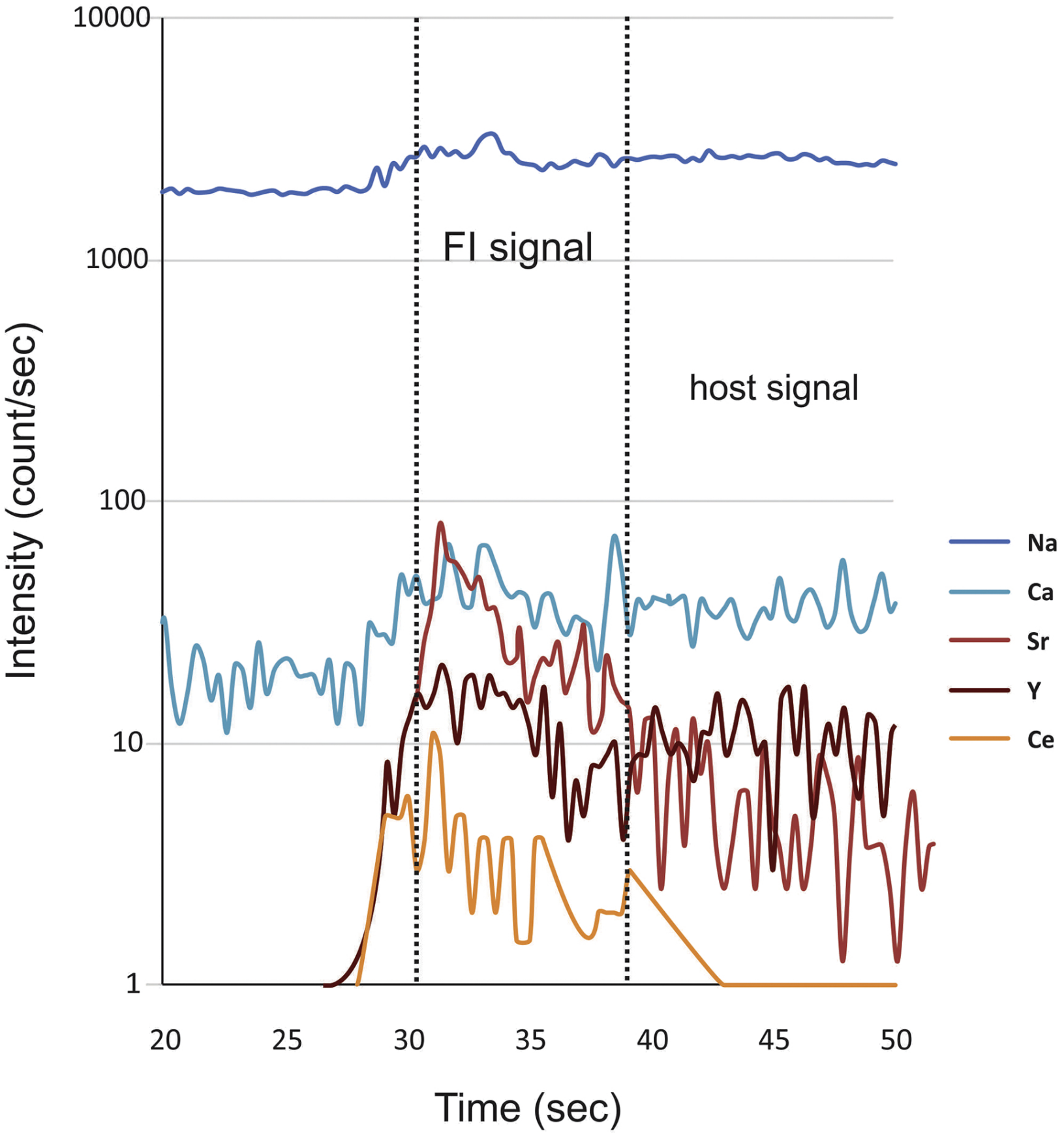
10000
1000
100
10
1
Intensity (count/sec)
FI signal
host signal
Na
Ca
Sr
Y
Ce
20
25
30
35
40
45
50
Time (sec)

Figure 10

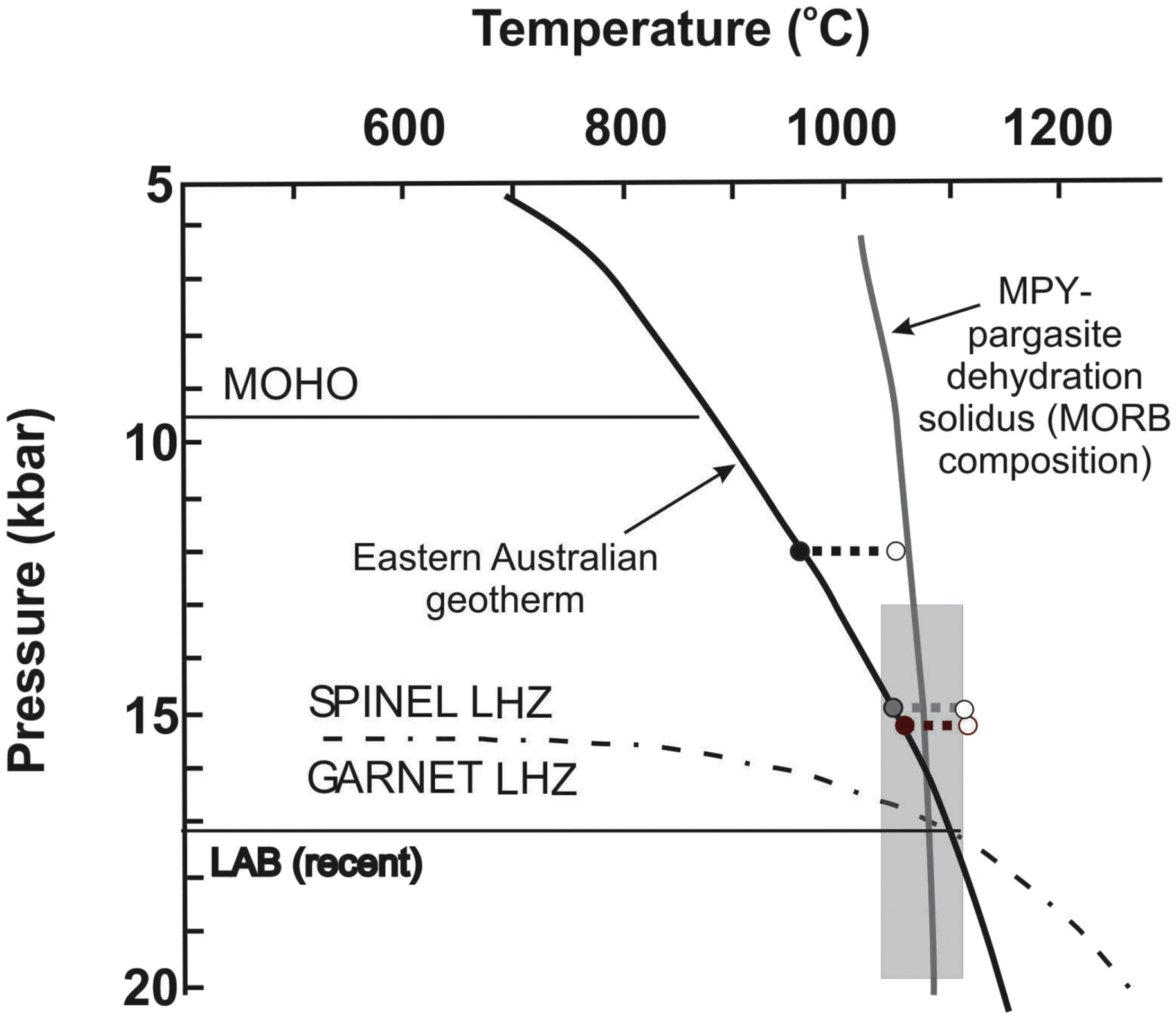
Temperature (°C)
600
800
1000
1200
5
10
15
20
Pressure (kbar)
MOHO
MPY-
pargasite
dehydration
solidus (MORB
composition)
Eastern Australian
geotherm
SPINEL LHZ
GARNET LHZ
LAB (recent)

Figure 11

A. extension by continental rifting

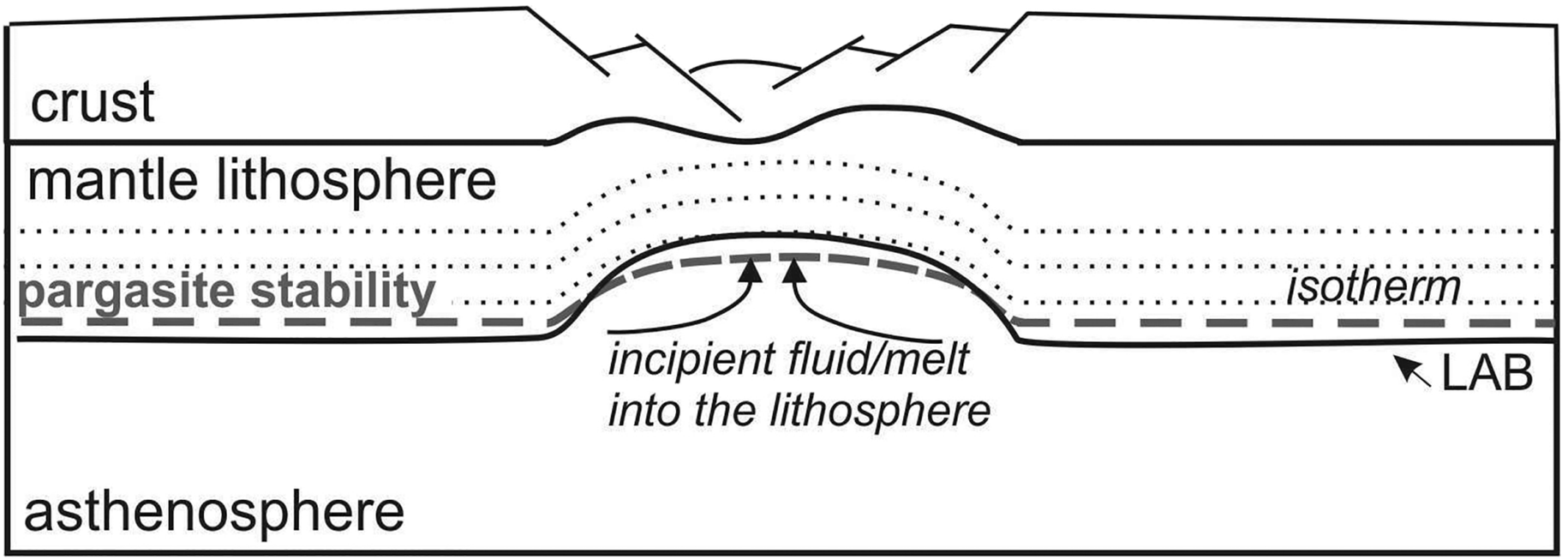

B. postrift thermal relaxation - cooling

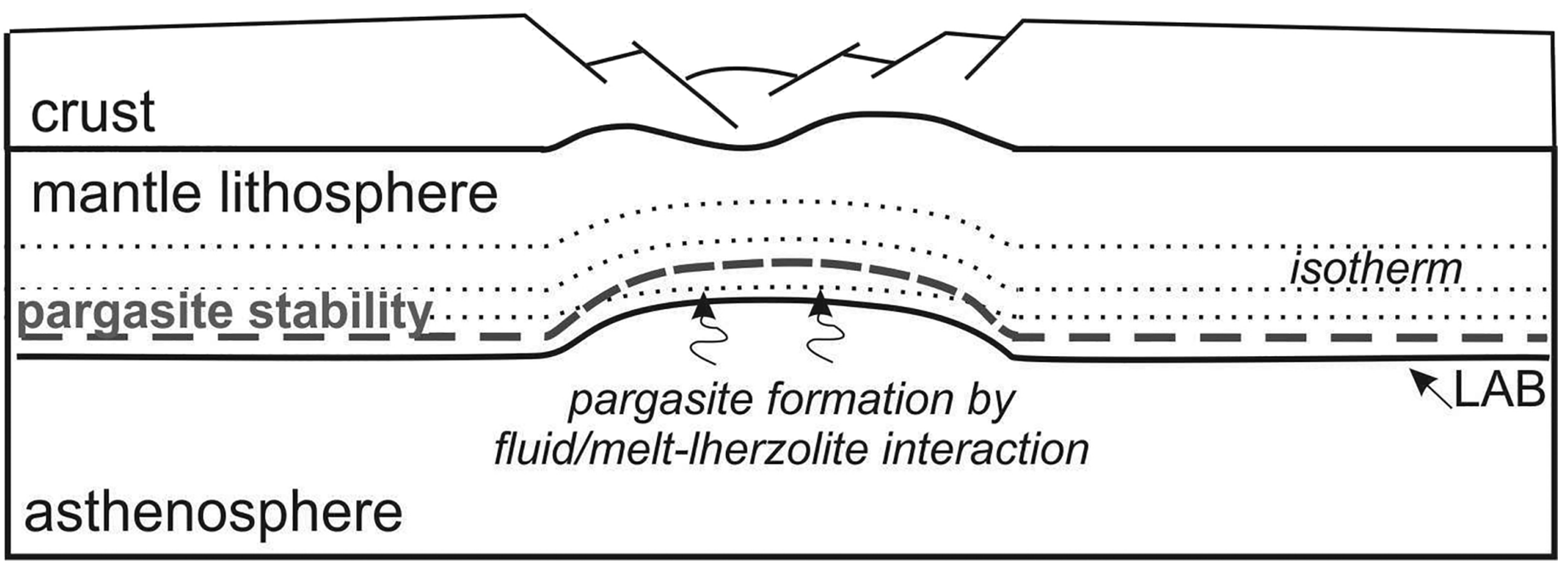

Figure 12